Chapter 7
Feedback Control

Feedback control is the most commonly used technique for eliminating positioning errors in nanopositioning systems. This chapter provides an overview of feedback control techniques with an experimental comparison of integral control, inversion-based control, and IRC damping control. When the reference trajectory is periodic, repetitive control (RC) can significantly improve the tracking performance of a feedback loop. The RC approach is introduced for nanopositioning.

7.1 Introduction

When operated in open-loop, the static accuracy of a nanopositioning system is limited by piezoelectric hysteresis, creep, cross-coupling from other axes, external disturbances, and temperature drift. To eliminate or reduce these error sources, nanopositioning systems require some form of feedback or feedforward compensation.

As illustrated in Fig. 7.1, a feedback controller works by comparing the commanded position to the actual displacement. By minimizing the positioning error, a feedback controller can compensate for all forms of positioning errors that are within its effective bandwidth. Due to the simplicity and ability to compensate for a wide range of errors, feedback controllers are commonly used in commercial nanopositioning systems.

In applications where fast changes in the reference siganl occur, large positioning errors can also arise from the mechanical resonances of the stage. To avoid excitation of the mechanical resonance in open-loop, the frequency of driving signals is limited to between 1 and 10 % of the resonance frequency (depending on the signal). In applications where the frequency of driving signals should be maximized, for example, in high-speed atomic force microscopy (Ando et al. 2005; Schitter et al. 2007; Humphris et al. 2005; Rost et al. 2005), the nanopositioner is operated in open-loop with driving signals that are shaped to reduce harmonic content. Although

A. J. Fleming and K. K. Leang, *Design, Modeling and Control of Nanopositioning Systems*, Advances in Industrial Control,
DOI: 10.1007/978-3-319-06617-2_7,

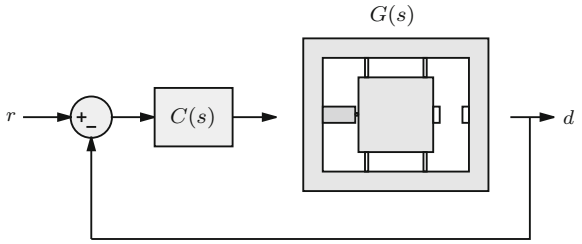

Fig. 7.1 A nanopositioner G in a displacement feedback control loop. The feedback controller $C(s)$ drives the nanopositioner $G(s)$ so that the difference between the reference r and measured position d is minimized

command shaping techniques, reviewed in (Fleming and Wills 2009), can provide a fast response, they do not account for nonlinearity or disturbances.

Since the first resonance mode typically dominates the response, the dynamics of a nanopositioner can be approximated by a second-order low-pass system

$$G(s) = \frac{\omega_n^2}{s^2 + 2\omega_n \zeta s + \omega_n^2}, \tag{7.1}$$

where ω_n and ζ are the natural frequency and damping ratio. Although a second-order system is a highly simplified model, it is sufficient to demonstrate the limitations experienced by some feedback controllers. The magnitude and phase responses of this system are plotted in Fig. 7.4.

The first closed-loop nanopositioning systems were piezoelectric tube scanners with capacitive (Griffith et al. 1990) or optical sensors (Barrett and Quate 1991). Although the early controllers were primarily manually tuned, model-based lead-lag and $\mathcal{H}_\infty$ controllers were also investigated (Tamer and Dahleh 1994).

To improve the gain-margin and closed-loop bandwidth of nanopositioning systems, notch filters or inversion filters can be effective (Leang and Devasia 2007). Such techniques can provide excellent closed-loop bandwidth, up to or greater than the resonance frequency (Abramovitch et al. 2008). However, to achieve high performance, an extremely accurate system model is required. Due to the dependency on model accuracy, a small change in the system dynamics can result in instability. For example, a resonance frequency reduction of 10 % may cause a high-gain inversion-based feedback controller to become unstable. In many applications, the high sensitivity to modeling error is unacceptable as the load mass and resonance frequency of a nanopositioner can vary significantly during service. As a result, high-performance inversion-based controllers are only applied in applications where the resonance frequency is stable, or when the feedback controller can be continually recalibrated (Abramovitch et al. 2008).

Damping control is an alternative method for reducing the bandwidth limitations imposed by mechanical resonance. Damping control uses a feedback loop to artificially increase the damping ratio of a system. With an integral controller, an increase

in ζ allows a proportional increase in the feedback gain and closed-loop bandwidth. Although damping controllers alone cannot increase the closed-loop bandwidth to beyond the resonance frequency, they have the advantage of being insensitive to variations in the resonance frequency. In addition, damping controllers suppress, rather than invert, the mechanical resonance so they can provide better rejection of external disturbances than inversion-based systems.

A number of techniques for damping control have been demonstrated successfully in the literature, these include positive position feedback (PPF) (Fanson and Caughey 1990), polynomial-based control (Aphale et al. 2008), shunt control (Fleming and Moheimani 2006; Fleming et al. 2002), resonant control (Sebastian et al. 2008), and integral resonance control (IRC) (Aphale et al. 2007; Bhikkaji and Moheimani 2008).

In Aphale et al. (2007), IRC was demonstrated as a simple means for damping multiple resonance modes of a cantilever beam. The IRC scheme employs a constant feedthrough term and a simple first-order controller to achieve substantial damping of multiple resonance modes. An adaption of this controller that is suitable for tracking control was reported in (Fleming et al. 2010). The regulator form of IRC is a first-order low-pass filter, which is straightforward to implement. A major benefit of the regulator form is that it can be enclosed in a simple tracking control loop to eliminate drift and effectively reduce nonlinearity at low frequencies.

Optimal controllers with automatic synthesis have also been successfully applied to nanopositioning applications. Examples include robust $\mathcal{H}_\infty$ controllers (Salapaka et al. 2002; Sebastian and Salapaka 2005) and LMI-based controllers (Lee and Salapaka 2009). Robust controllers have also been incorporated with approximate models of hysteresis to improve performance (Chen 1992).

Other control techniques include methods that are targeted at particular trajectories, such as triangular scanning signals (Eielsen et al. 2011). Such periodic reference trajectories often arise in nanopositioning applications (Kenton and Leang 2012). A commonly used technique for controlling systems with periodic inputs or disturbances is RC, as discussed in Sect. 7.10. Another technique that can be used to improve the reference tracking performance of a feedback system is feedforward control (Wu and Zou 2009; Leang and Devasia 2007), which is discussed in Chap. 9.

In the following, an experimental nanopositioner is described for the purpose of examining the performance of three practical controllers. In Sect. 7.3, the performance limitations of basic integral control are discussed. This is followed by a description of inverse control and damping control in Sects. 7.4 and 7.5. In Sect. 7.6, the bandwidth, settling time, and robustness of the three controllers are compared. Each controller is designed to maximize bandwidth while retaining stability margins of at least 6 dB and 60°.

Scanning probe microscopy is an application that requires high-performance control of the sample and probe nanopositioner. The performance implications of each control strategy are demonstrated by applying each technique to an atomic force microscope in Sect. 7.9.

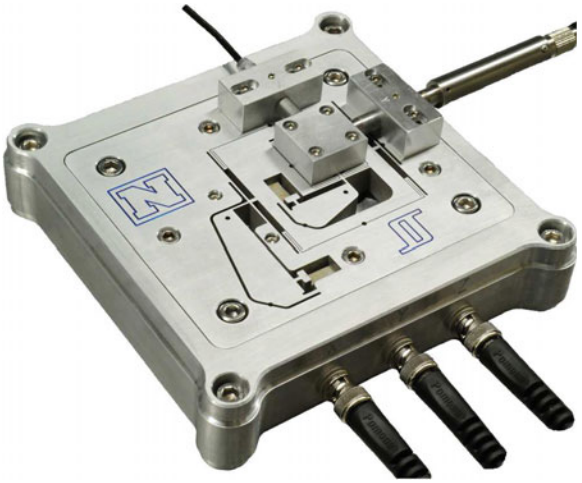

Fig. 7.2 A two-axis serial kinematic nanopositioning platform with a range of 30 μm

7.2 Experimental Setup

To compare the controller characteristics, each technique will be applied to the XY lateral nanopositioning stage pictured in Fig. 7.2. Each axis contains a 12 mm piezoelectric stack actuator (Noliac NAC2003-H12) with a free displacement of 12 μm at 200 V. The flexure design includes a mechanical amplifier to provide a total range of 30 μm. The flexures also mitigate cross-coupling between the axes so that each axis can be controlled independently. The position of the moving platform is measured by a Microsense 6810 capacitive sensor and 6504-01 probe, which has a sensitivity of 2.5 μm/V. The stage is driven by two PiezoDrive PDL200 voltage amplifiers with a gain of 20.

The x-axis, which translates from left to right in Fig. 7.2, has a resonance frequency of 513 Hz. The y-axis contains less mass so the resonance frequency is higher, 727 Hz. Since the x-axis imposes a greater limitation on performance, the comparison will be performed on this axis. However, the design process for the other axis is identical.

The frequency response for a nominal load is plotted in Fig. 7.3a. With the maximum payload, the resonance frequency reduces to 415 Hz as shown in Fig. 7.3b. It can be observed that payload mass significantly modifies the higher frequency dynamics.

For the purpose of control design, a second-order model is procured using the frequency domain least-squares techniques. The model parameters are:

$$G(s) = \frac{2.025 \times 10^7}{s^2 + 48.63s + 1.042 \times 10^7}. \tag{7.2}$$

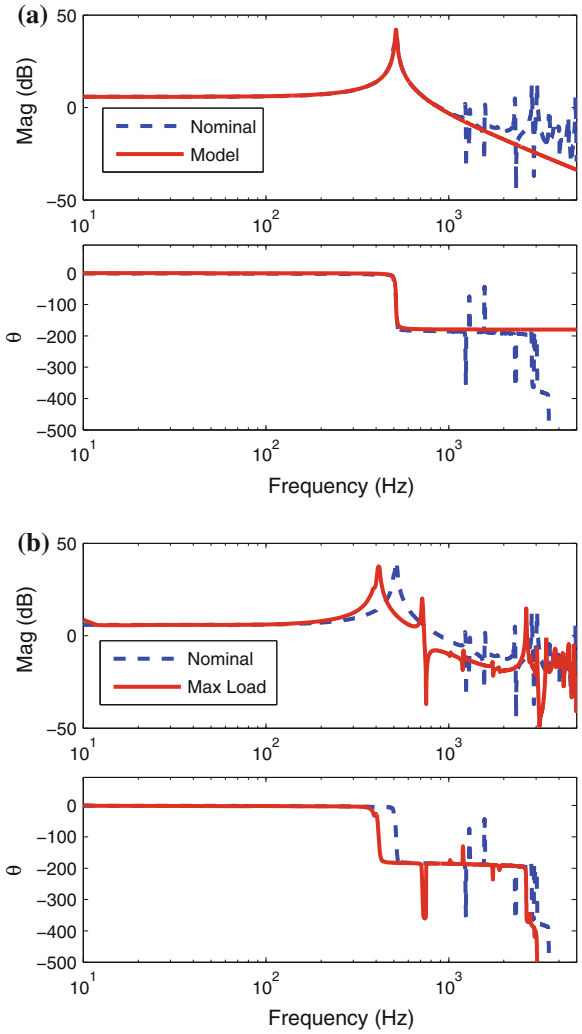

Fig. 7.3 The open-loop frequency response measured from the voltage amplifier input to the sensor output, scaled to μm/V. In **a** the nominal response is compared to the identified model. In **b** the frequency response of the system with maximum load is compared to the nominal response

The frequency response of the model is compared to the experimental data in Fig. 7.3a. The model closely approximates the first resonance mode, which is sufficient for control design.

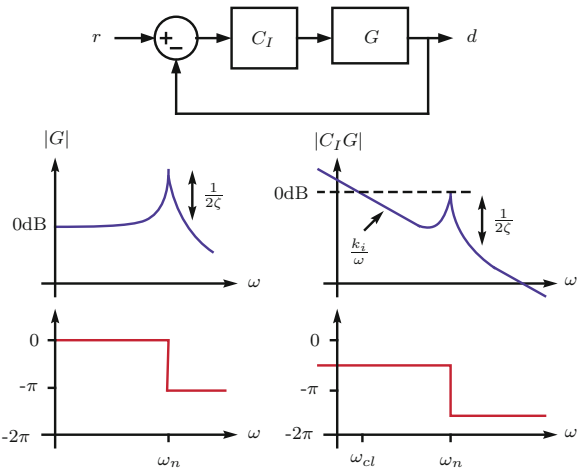

Fig. 7.4 A nanopositioning system G controlled by an integral controller $C_I = k_i/s$. The frequency response of G and the system loop-gain $C_I G$ are plotted on the *left* and *right hand side* respectively

7.3 PI Control

A popular technique for control of commercial nanopositioning systems is sensor-based feedback using integral or proportional-integral control (Li et al. 2006). The transfer function of a PID controller is

$$C_{\text{PID}}(s) = k_p + k_i/s + k_d s, \tag{7.3}$$

However, the derivative term is rarely used due to the increased noise sensitivity and stability problems associated with high frequency resonance modes. PI controllers are simple to tune and effectively reduce piezoelectric nonlinearity at low frequencies. However, the bandwidth of PI tracking controllers is severely limited by the presence of highly resonant modes. The limited closed-loop bandwidth can be explained by examining the loop gain $C_I G$ in Fig. 7.4. Here, the resonant system G is controlled by an integral controller C_I with gain k_i. The factor limiting the maximum feedback gain and closed-loop bandwidth is gain-margin.

Above the natural frequency ω_n, which is approximately equal to the resonance frequency in systems with low damping, the phase lag of the loop-gain exceeds π so the magnitude must be less than 1 (0 dB) for stability in closed-loop. The condition for closed-loop stability is approximately

$$\frac{k_i}{\omega_n} \times \frac{1}{2\zeta} < 1, \text{ or } k_i < 2\omega_n \zeta. \tag{7.4}$$

As the system G is unity gain, the complementary sensitivity function is

$$\frac{d(s)}{r(s)} = \frac{C_I(s)G(s)}{C_{PI}(s)G(s)+1} \approx \frac{k_i}{s+k_i}. \tag{7.5}$$

Thus, the feedback gain k_i is also the approximate 3-dB bandwidth of the complementary sensitivity function and the 0-dB crossing of the loop-gain (in radians per second). From this fact, and the stability condition (7.4), the maximum closed-loop bandwidth is equal to twice the product of damping ratio ζ and natural frequency ω_n, i.e.,

$$\text{max. closed-loop bandwidth} < 2\omega_n\zeta. \tag{7.6}$$

This is a severe limitation as the damping ratio is usually on the order of 0.01, so the maximum closed-loop bandwidth is less than 2 % of the resonance frequency. If a certain amount of gain-margin is required, the bandwidth further reduces to:

$$\text{max. closed-loop bandwidth} < \frac{2\omega_n\zeta}{\text{gain-margin}}, \tag{7.7}$$

where the gain margin is specified as a linear magnitude rather than in dB, for example, 2 rather than 6 dB. The maximum closed-loop bandwidth can also be estimated directly from the frequency response by replacing the factor 2ζ with $1/P$, where P is the linear magnitude of the resonance peak divided by the DC gain, that is

$$\text{max. closed-loop bandwidth} < \frac{\omega_n}{P \times \text{gain-margin}}, \tag{7.8}$$

Due to the second-order resonance, adding a first-order zero to the loop-gain with a proportional term offers little improvement. A derivative term can be beneficial, however this is rarely used as it can destabilize higher frequency modes. A better alternative to derivative action is the notch filter or damping controller discussed in the following sections.

For the nanopositioner under consideration, an integral gain of 15.5 results in a gain-margin of 6 dB and a bandwidth of 13 Hz. The performance is compared to the inversion and damping controllers in Sect. 7.6.

7.4 PI Control with Notch Filters

Techniques aimed at improving the closed-loop bandwidth are typically based on either inversion of resonant dynamics using a notch filter (Abramovitch et al. 2008; Leang and Devasia 2007) or the use of a damping controller (Fleming et al. 2010; Aphale et al. 2008). Inversion techniques are popular as they are simple to implement and can provide a high closed-loop bandwidth if they are finely tuned and the resonance frequency does not vary (Abramovitch et al. 2008). The transfer function of a typical inverse controller is

$$C_{\text{Notch}}(s) = \left(k_p + \frac{k_i}{s}\right) \frac{s^2 + 2\omega_z\zeta_z s + \omega_z^2}{\omega_z^2} \tag{7.9}$$

where ζ_z and ω_z are approximately the damping ratio and first resonance frequency of the nanopositioner. Depending on the implementation method, an additional pole may be required above the bandwidth of interest in order to ensure causality.

The direct inversion controller (7.9) may not be suitable when significant higher-frequency resonances exist. In this case, a notch filter is more appropriate since it attempts to replace the lightly damped resonance with a pair of real poles. Other denominator posibilities include, for example, a pair of complex poles with critical damping. The transfer function is

$$C_{\text{Notch}}(s) = \left(k_p + \frac{k_i}{s}\right) \frac{s^2 + 2\omega_z\zeta_z s + \omega_z^2}{(s + \omega_z)^2} \tag{7.10}$$

If an inverse controller is precisely tuned to the first mechanical resonance, the presence of this mode can be essentially eliminated from the loop-gain. The maximum bandwidth is now limited by the second system resonance rather than the first. Equations (7.7) or (7.8) predict the maximum closed-loop bandwidth based on the resonance frequency and damping ratio of the second significant resonance mode. Additional notch filters can be used to invert higher order resonances, however this requires an extremely accurate system model.

A major consideration with inversion-based control is the possibility for modeling error. In particular, if the resonance frequency drops below the frequency of the notch filter, the phase lag will cause instability. Therefore, a notch filter must be tuned to the lowest resonance frequency that will occur during service. For example, the nanopositioner under consideration has a nominal resonance frequency of 513 Hz and a minimum resonance frequency 410 Hz. Thus, the notch filter is tuned to 410 Hz with an estimated damping of $\zeta_z = 0.01$.

To maintain a gain-margin of 6 dB, the maximum integral gain is $k_i = 44$. The loop-gain during nominal and maximum load conditions is plotted in Fig. 7.5. During nominal conditions, the phase-lag does not exceed 180° until the second resonance mode; however, the first resonance mode remains dominant in the response and can be excited by high-frequency components of the input or disturbances. This behavior is evident in the closed-loop frequency and step responses plotted in Sect. 7.6. Since the notch filter is tuned to the lowest resonance frequency, the system actually performs better with the maximum payload. The loop-gain in Fig. 7.5 shows that the first resonance-mode is almost inverted during this condition.

Due to the sensitivity of inversion-based controllers to variations in the resonance frequency, they are most suited to applications where the resonance frequency is stable, or where the feedback controller can be continually recalibrated (Abramovitch et al. 2008).

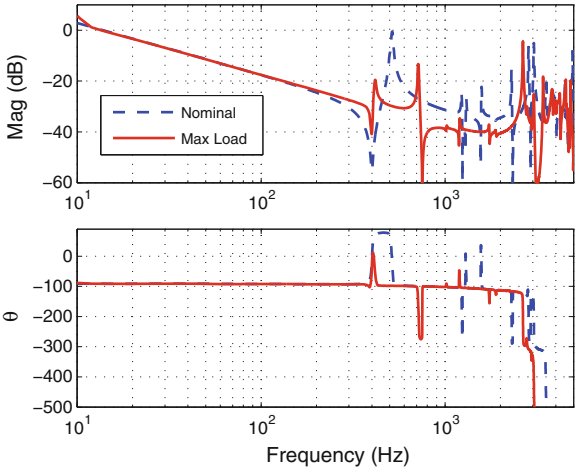

Fig. 7.5 The loop-gain of the nanopositioner and inversion based controller during nominal and maximum load ($C_{\text{notch}}(s)G(s)$)

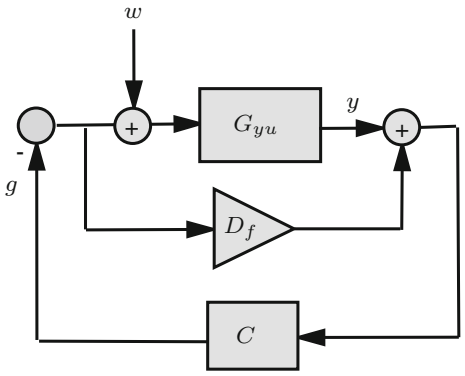

Fig. 7.6 Integral resonance control scheme (Aphale et al. 2007)

7.5 PI Control with IRC Damping

Integral Resonance Control (IRC) was introduced in 2007 as a means for augmenting the structural damping of resonant systems with collocated sensors and actuators (Aphale et al. 2007). A diagram of an IRC loop is shown in Fig. 7.6. It consists of the collocated system G_{yu}, an artificial feedthrough D_f and a controller C. The input disturbance w represents environmental disturbances but can also be used to obtain some qualitative information about the closed-loop response to piezoelectric nonlinearity. That is, if the disturbance rejection at the scan frequency and first few harmonics is large, a significant reduction in hysteresis could be expected.

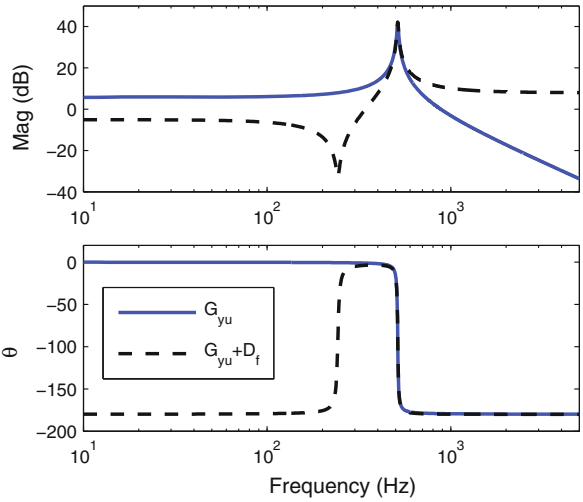

Fig. 7.7 Frequency response of the open-loop system G_{yu} and with artificial feedthrough $G_{yu}+D_f$, where $D_f = -2.5$. The 180° phase change of $G_{yu} + D_f$ is due to the negative feedthrough which also makes the system inverting

The first step in designing an IRC controller is to select, and add, an artificial feedthrough term D_f to the original plant G_{yu}. The new system is referred to as $G_{yu}+D_f$. It has been shown that a sufficiently large and negative feedthrough term will introduce a pair of zeros below the first resonance mode and also guarantee zero-pole interlacing for higher frequency modes (Aphale et al. 2007). Smaller feedthrough terms permit greater maximum damping. Although it is straightforward to manually select a suitable feedthrough term, it can also be computed from Theorem 2 in (Aphale et al. 2007).

For the model G_{yu} described in (7.2), a feedthrough term of $D_f = -2.5$ is sufficient to introduce a pair of zeros below the first resonance mode. The frequency responses of the open-loop system G_{yu} and the modified transfer function $G_{yu} + D_f$ are plotted in Fig. 7.7.

The key behind IRC is the phase response of $G_{yu} + D_f$, which now lies between between $-180°$ and $0°$ as shown in Fig. 7.7. Due to the bounded phase of $G_{yu} + D_f$ a simple negative integral controller

$$C = \frac{-k}{s}, \tag{7.11}$$

can be applied directly to the system. To examine the stability of such a controller, we consider the loop-gain $C \times \left(G_{yu} + D_f\right)$. For stability, the phase of the loop-gain must be within $\pm 180°$ while the gain is greater than zero. The phase of the loop-gain $C \times \left(G_{yu} + D_f\right)$ is equal to the phase of $G_{yu}+D_f - 180°$ for the negative controller gain and a further $90°$ for the single controller pole. The resulting phase response

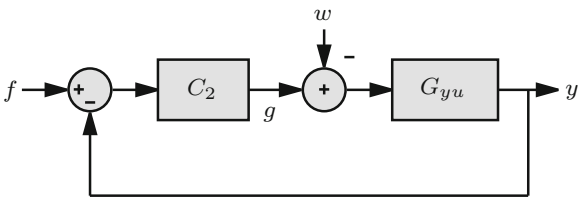

Fig. 7.8 The integral resonance controller of Fig. 7.6 rearranged in regulator form

of the loop-gain lies between $+90°$ and $-90°$. That is, regardless of controller gain, the closed-loop system has a phase margin of $90°$ and an infinite gain-margin with respect to $G_{yu} + D_f$.

A suitable controller gain k can be selected to maximize damping using the root-locus technique (Aphale et al. 2007). For the system under consideration, a gain of $k = 1{,}900$ results in a maximum damping ratio 0.57.

In order to facilitate a tracking control loop, the feedback diagram must be rearranged in a form where the input does not appear as a disturbance. This can be achieved by finding an equivalent regulator that provides the same loop gain, as shown in Fig. 7.8. In Fig. 7.6, the control input g is related to the measured output y by

$$g = C(y - D_f g), \tag{7.12}$$

thus, the equivalent regulator C_2 is

$$C_2 = \frac{C}{1 + CD_f}. \tag{7.13}$$

When $C = \frac{-k}{s}$ the equivalent regulator is

$$C_2 = \frac{-k}{s - kD_f}. \tag{7.14}$$

The closed-loop transfer function of the damping loop is,

$$G_{yf} = \frac{G_{yu}C_2}{1 + G_{yu}C_2}. \tag{7.15}$$

With $D_f = -2.5$ and $k = 1{,}900$, the frequency responses of the open-loop and damped system are plotted in Fig. 7.9.

To achieve integral tracking action, the IRC loop can be enclosed in an outer loop as shown in Fig. 7.10. From the response in Fig. 7.9 or a pole-zero map, it can be observed that the damped system contains the resonance poles, plus an additional first-order pole mid-way between the resonance frequency and the zeros of $G_{yu}+D_f$. To eliminate the additional pole from the loop-gain, an ideal tracking controller is a

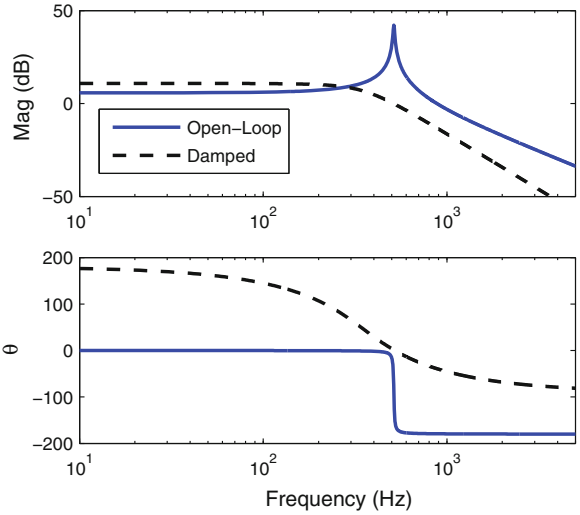

Fig. 7.9 The open- and closed-loop frequency response of the system with integral resonance control

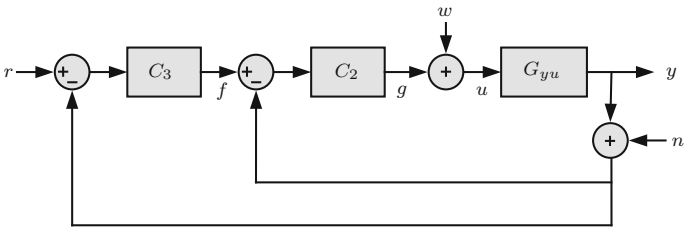

Fig. 7.10 Tracking control system with the damping controller $C_2(s)$ and tracking controller $C_3(s)$. The signal w is the disturbance input and n is the sensor noise

PI controller with a fixed zero at the frequency of the additional pole, that is,

$$C_3 = \frac{-k_i(s+\omega_z)}{s\omega_z}. \tag{7.16}$$

where k_i is chosen in the normal way to provide the desired stability margins or bandwidth. Note that C_3 is inverting to cancel the inverting nature of G_{yf}. For the system under comparison, a gain of $k_i = 245$ results in a phase margin of 60°. The closed-loop response performance is examined in Sect. 7.6.

The transfer function of the closed-loop system is

$$\frac{y}{r} = \frac{C_3 G_{yf}}{1 + C_3 G_{yf}}, \tag{7.17}$$

Table 7.1 Summary of controller parameters

	PI	PI + Notch	PI + IRC
Tracking TF	$\frac{15.5}{s}$	$\frac{44}{s}\frac{2\pi 10^3}{s+2\pi 10^3}$	$\frac{-245}{s}\frac{s+2720}{2720}$
Inverse or damping TF	–	$\frac{s^2+50.27s+6.317\times 10^6}{6.317\times 10^6}$	$\frac{-1900}{s+4750}$

or alternatively,

$$\frac{y}{r} = \frac{C_2C_3G_{yu}}{1 + C_2(1 + C_3)G_{yu}}. \tag{7.18}$$

In addition to the closed-loop response, the transfer function from disturbance to the regulated variable y is also of importance,

$$\frac{y}{w} = \frac{G_{yu}}{1 + C_2(1 + C_3)G_{yu}}. \tag{7.19}$$

That is, the disturbance input is regulated by the equivalent controller $C_2(1 + C_3)$.

7.6 Performance Comparison

In Sects. 7.3–7.5, three controllers were designed to maintain a gain and phase margin of at least 6 dB and 60°. The controller parameters are summarized in Table 7.1, and the simulated stability margins are listed in Table 7.2. The integral and inverse controller were limited by gain-margin while the damping controller was limited by phase margin.

The simulated and experimental closed-loop frequency responses are plotted in Figs. 7.11 and 7.12. The frequency where the phase-lag of each control loop exceeds 45° is compared in Table 7.2. In nanopositioning applications, the 45° bandwidth is more informative than the 3 dB bandwidth since it is more closely related to the settling time. Due to the higher permissible servo gain, the PI + IRC controller provides the highest bandwidth by a significant margin.

The simulated and experimental step responses are plotted in Figs. 7.13 and 7.14 and summarized in Table 7.2. The PI+IRC controller provides the shortest step response by approximately a factor of 5, however the response exhibits some overshoot.

Out of the three controllers, the combination of PI control and IRC provides the best closed-loop performance under both nominal and full-load conditions. This is the key benefit of damping control, it is more robust to changes in resonance frequency than inverse control. If the variation in resonance frequency were less, or if the resonance frequency was stable, there would not be a significant difference between the dynamic performance of an inverse controller and damping controller.

Table 7.2 Closed-loop performance summary of integral, inversion based, and damping controller

	PI	PI + Notch	PI + IRC
Gain margin			
Nominal load (dB)	6.1	6.0	14
Full load (dB)	7.0	5.1	10
Phase margin			
Nominal load	inf	89°	69°
Full load (°)	90	89	69
Nominal bandwidth (45°)			
Simulated (Hz)	4.8	13	74
Experimental (Hz)	5.0	13	50
Full-load bandwidth (45°)			
Simulated (Hz)	4.8	13	77
Experimental (Hz)	5.0	13	78
Nominal settling time (99 %)			
Simulated (ms)	160	54	6.2
Experimental (ms)	164	48	9.7
Full-load settling time (99 %)			
Simulated (ms)	170	53	11
Experimental (ms)	165	42	7.6

Since the damping controller requires more design effort than an inverse controller, it is sensible to choose this option when some variation in the resonance frequencies are expected, or if there are multiple low-frequency resonances that are difficult to model.

7.7 Noise and Resolution

The noise sensitivity of each control strategy is the transfer function from the sensor noise n to the actual position y. For the sake of comparison, the noise contribution of the voltage amplifier is assumed to be small compared to the sensor noise. As discussed in Chap. 13, the RMS value or standard deviation of the sensor-induced noise is equal to

$$\sigma = \sqrt{\int_0^\infty S_n(f) \left| \frac{y(2\pi jf)}{n(2\pi jf)} \right|^2 df}, \tag{7.20}$$

where $S_n(f)$ is the power spectral density of the sensor noise. If the sensor noise is Gaussian distributed, the resolution is equal to 6σ. Therefore, if the sensor noise spectral density is constant, the closed-loop resolution is proportional to the area under the noise sensitivity transfer function.

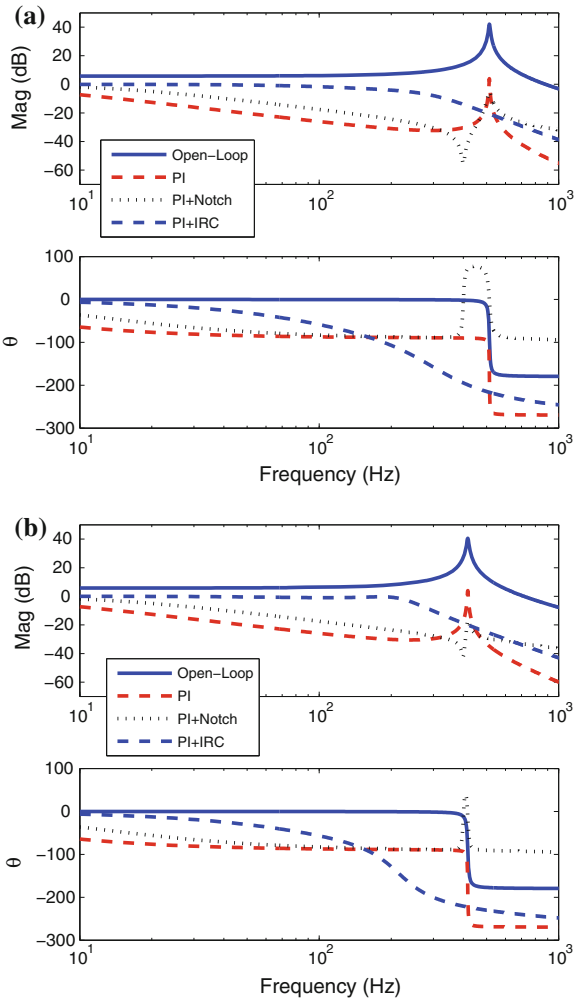

Fig. 7.11 The simulated closed-loop frequency response of each controller under nominal and maximum load conditions. **a** Nominal load, $f_r = 513\,\text{Hz}$. **b** Maximum load, $f_r = 415\,\text{Hz}$

For the PI and inverse controller, the noise sensitivity is the complementary sensitivity function with opposite sign, that is

$$\frac{y}{n} = \frac{-C_3 G_{yu}}{1 + C_3 G_{yu}}. \tag{7.21}$$

However, with a damping controller as shown in Fig. 7.10, the noise sensitivity is not identical to the complementary sensitivity (7.17). Rather, it is

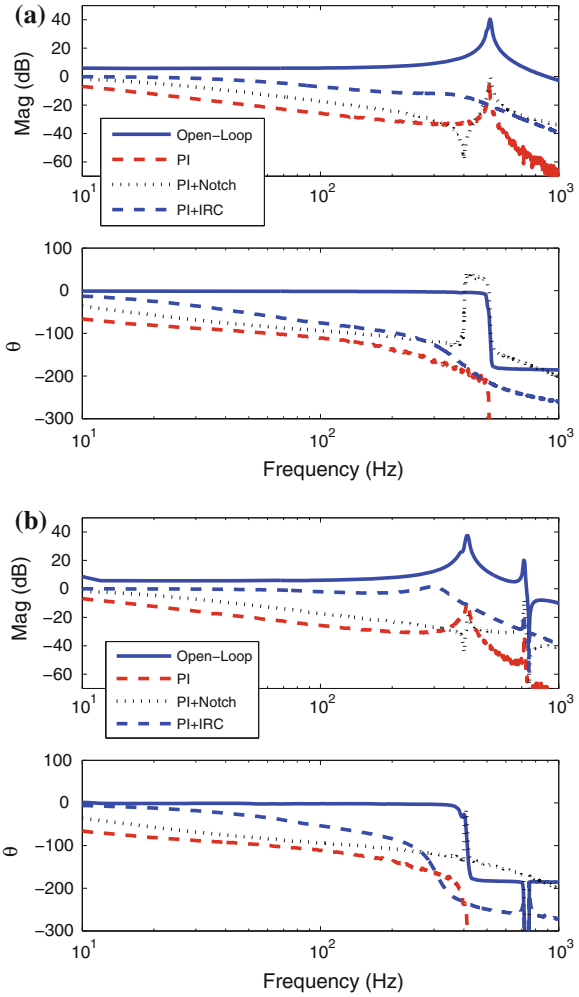

Fig. 7.12 The experimental closed-loop frequency response of each controller under nominal and maximum load conditions. **a** Nominal load, $f_r = 513\,\text{Hz}$. **b** Maximum load, $f_r = 415\,\text{Hz}$

$$\frac{y}{n} = \frac{-C_2(1+C_3)G_{yu}}{1+C_2(1+C_3)G_{yu}}. \tag{7.22}$$

It can be observed from Eq. (7.21) that the noise sensitivity for a standard control loop can be reduced by reducing the closed-loop bandwidth or controller gain. However with a damping controller, the noise sensitivity bandwidth is dominated by the damping control loop, not the tracking loop. This is a drawback since the noise sensitivity bandwidth cannot be reduced by varying the tracking controller gain. However, since the noise sensitivity of the IRC system is not strongly affected by the tracking

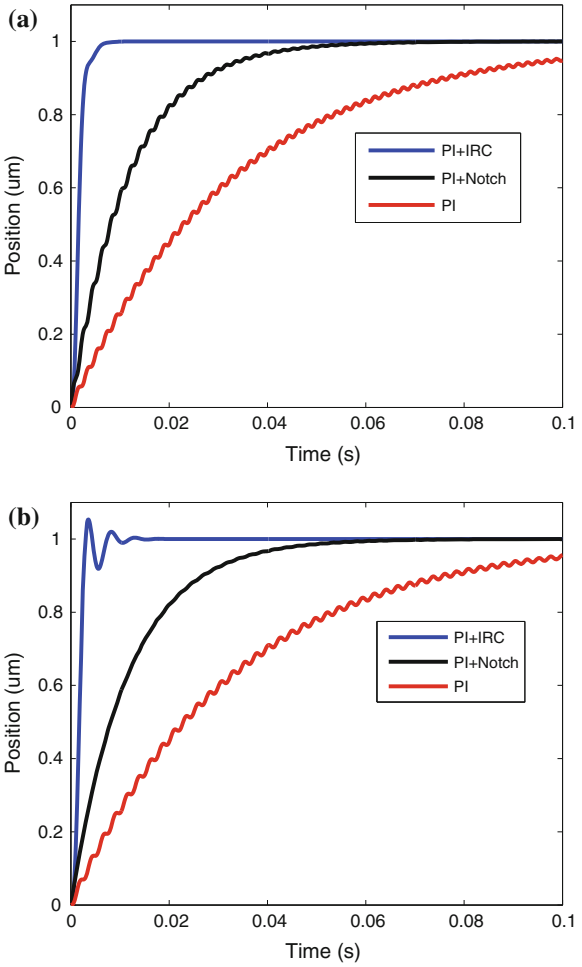

Fig. 7.13 The simulated closed-loop step response of each controller under nominal and maximum load conditions. **a** Nominal load, $f_r = 513\,\text{Hz}$. **b** Maximum load, $f_r = 415\,\text{Hz}$

controller gain C_3, the tracking controller can be tuned to the highest practical gain since there is little noise penalty in doing so.

The noise sensitivity of each control strategy is plotted in Fig. 7.15. Due to the wide bandwidth of the damping controller, the noise sensitivity bandwidth is significantly greater than the PI and inverse controllers.

A straightforward technique for estimating the positioning resolution is to measure the sensor noise and filter it by the noise sensitivity function. Following the guidelines in Sect. 13.9.3, the sensor noise was amplified using an SR560 amplifier with a gain of 10,000 and a bandwidth of 0.03–10 kHz. A 100 s of data was recorded at a sampling rate of 30 kHz. A 3 s record of the closed-loop position noise for each controller

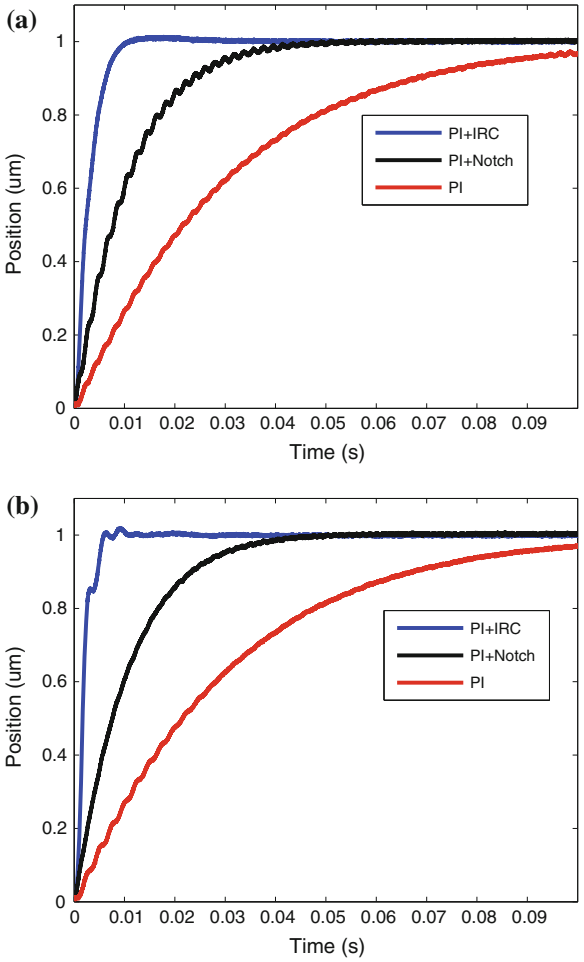

Fig. 7.14 The experimental closed-loop step response of each controller under nominal and maximum load conditions. **a** Nominal load, $f_r = 513\,\text{Hz}$. **b** Maximum load, $f_r = 415\,\text{Hz}$

is plotted in Fig. 7.16. While the PI and inverse controller contain low-frequency noise plus randomly excited resonance, the IRC controller results in a more uniform spectrum but with a wider noise bandwidth. Considering that the IRC controller increases the closed-loop bandwidth from 5 to 78 Hz (compared to PI control), the decrease in resolution from 0.27 to 0.43 nm is small.

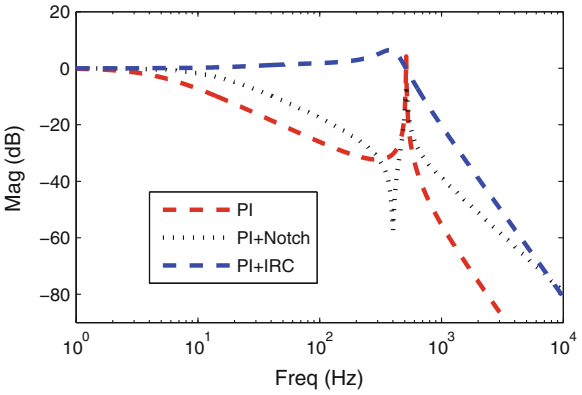

Fig. 7.15 The noise sensitivity of each control strategy

7.8 Analog Implementation

Due to the simplicity of the IRC damping and tracking controller, it is straightforward to implement in both analog and digital form. The IRC damping and tracking controller shown in Fig. 7.10 can be implemented directly with the analog circuit shown in Fig. 7.17. Although the controller requires only two opamps, the four-opamp circuit shown in Fig. 7.17 is easier to understand, trouble-shoot, and tune (if necessary).

The operation of the circuit is self-explanatory. The first stage is a unity-gain differential amplifier that implements the subtraction function $r - y$. The second stage implements the PI tracking controller. The corresponding circuit transfer function of the PI controller is

$$C_3(s) = -\frac{s + \frac{1}{r_{3b}c_3}}{r_{3a}c_3 \frac{1}{r_{3b}c_3} s}, \tag{7.23}$$

which results in the equality $r_{3a}c_3 = 1/k_i$ and $r_{3b}c_3 = 1/\omega_z$

The third stage is a unity-gain differential amplifier with two noninverting inputs for f and u_f. The final stage implements the IRC controller C_2, where

$$C_2(s) = \frac{-k}{s - kD_f}. \tag{7.24}$$

The circuit transfer function is

$$C_2(s) = \frac{-\frac{1}{r_{2a}c_2}}{s + \frac{1}{r_{2b}c_2}}. \tag{7.25}$$

As k is positive and D_f is negative, the equalities are

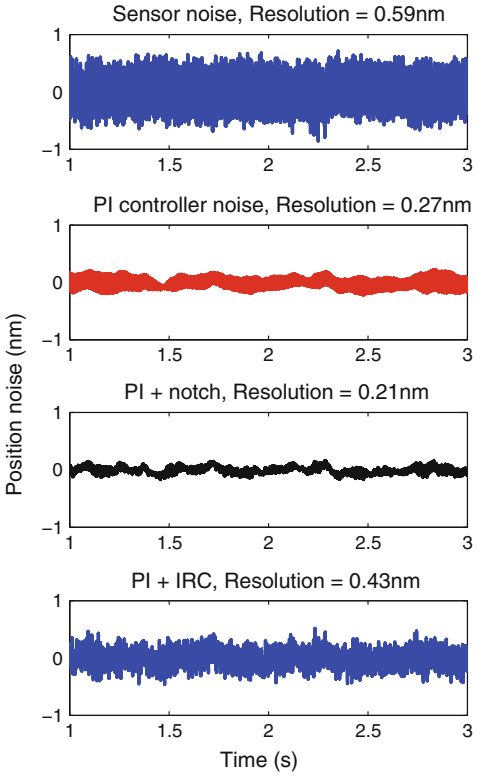

Fig. 7.16 The closed-loop noise of each control strategy and the corresponding 6σ-resolution

$$r_{2a}c_2 = \frac{1}{k}, \text{ and } r_{2b}c_2 = \frac{1}{kD_f}. \tag{7.26}$$

In both of the integrating stages, a 100 nF film capacitor (e.g., Polypropylene) is recommended as these capacitors are highly linear and temperature stable. The capacitance value should not be less than 100 nF to avoid large resistances that contribute thermal noise and amplify current noise. The opamps should have a gain-bandwidth product of around 10 Mhz or greater to avoid controller phase lag. The opamps should also be suited to a source impedance in the kΩ range with the lowest possible noise corner frequency. The Texas Instruments OPA4227 is a suitable device, which is readily available at low cost.

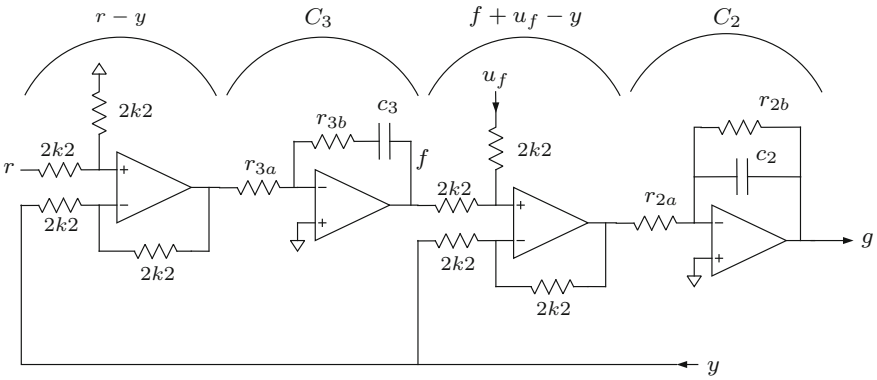

Fig. 7.17 Analog implementation of an IRC damping and PI tracking controller

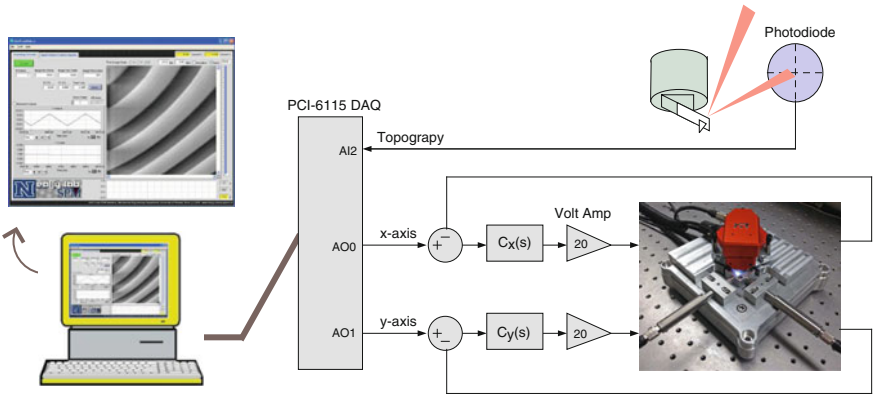

Fig. 7.18 The AFM system in constant-height contact-mode. A lab view application creates the scanning waveforms and records the image while an xPC Target performs the real-time control

7.9 Application to AFM Imaging

To illustrate the impact of positioning bandwidth on application performance, the nanopositioner will be employed for lateral scanning in an atomic force microscope (Abramovitch et al. 2007; Salapaka and Salapaka 2008; Ando et al. 2008; Schitter 2009; Clayton et al. 2009; Fleming et al. 2010).

The experimental setup is shown in Fig. 7.18. A National Instruments PCI-6115 data acquisition card and LabView application[1] are used to generate the raster signals and acquire the image (Fleming et al. 2010). The AFM head is a NanoSurf EasyScan microscope which is only used for holding the cantilever and measuring the deflection. The microcantilver is a Budget Sensors ContAl cantilever with a stiffness of

[1] The easyLab SPM Interface is available by contacting K. K. Leang at kam@unr.edu.

0.2 N/m and the sample under consideration is a silicon calibration grating with a period of 6 μm and a height of 20 nm.

The scan waveforms are standard triangular raster signals. To acquire an image, the y-axis is driven with a slow ramp while the x-axis reference is a 10 Hz triangular waveform. With a scan rate of 10 Hz, a 200 × 200 pixel image is acquired in 20 s. Due to the slow scan rate of the y-axis, the tracking error can be neglected. However, significant positioning errors can arise from the x-axis response. The positioning error for each controller and the resulting image is plotted in Fig. 7.19. The higher bandwidth of the IRC control system is observed to significantly reduce scan-induced imaging artifacts.

7.10 Repetitive Control

7.10.1 Introduction

Many applications in nanopositioning require the stage to track periodic reference trajectories with precision. For example, in AFM a nanopositioner is used to raster back and forth a probe tip relative to a sample surface to obtain high-resolution topographical images, directly measure various properties of a specimen, and even investigate nano-scale dynamic interactions in real time (Radmacher 1997; Salapaka and Salapaka 2008; Ando et al. 2008). The periodicity of the desired trajectory lends itself nicely for applying RC for precision positioning, even at relatively high speed. Recently, the RC approach has been applied to piezo-based positioners and SPMs (Aridogan et al. 2009; Merry et al. 2011; Shan and Leang 2012a, b, 2013).

Repetitive control (RC) is a direct application of the internal model principle (Francis and Wonham 1976), where a signal generator—the transfer function of the reference trajectory—is incorporated into a feedback loop to provide high gain at the fundamental frequency of the reference trajectory and its harmonics (Inoue et al. 1981; Hara et al. 1988). Repetitive controllers have been used to address run-out issues in disk drive systems (Chew and Tomizuka 1990; Steinbuch et al. 2007) and to improve the performance of machine tools (Li and Li 1996; Chen and Hsieh 2007). Compared to traditional proportional-integral or proportional-integral-derivative (PID) feedback controllers, where careful tuning is required and the residual tracking error persists from one operating cycle to the next, RC has the ability to reduce the error as the number of operating cycles increases. For applications in which the desired trajectory is periodic and the signal period is known a priori, a repetitive controller offers many advantages. First, it can be plugged into an existing feedback control loop to enhance performance for scanning applications. Second, compared to iterative learning control (ILC) (Arimoto et al. 1984; Moore et al. 1992), a control method that has been used extensively for piezo-based positioning systems (Leang and Devasia 2006; Wu and Zou 2007), RC does not require the initial condition to be reset at the start of each iteration trial (Hara et al. 1988). Therefore, the

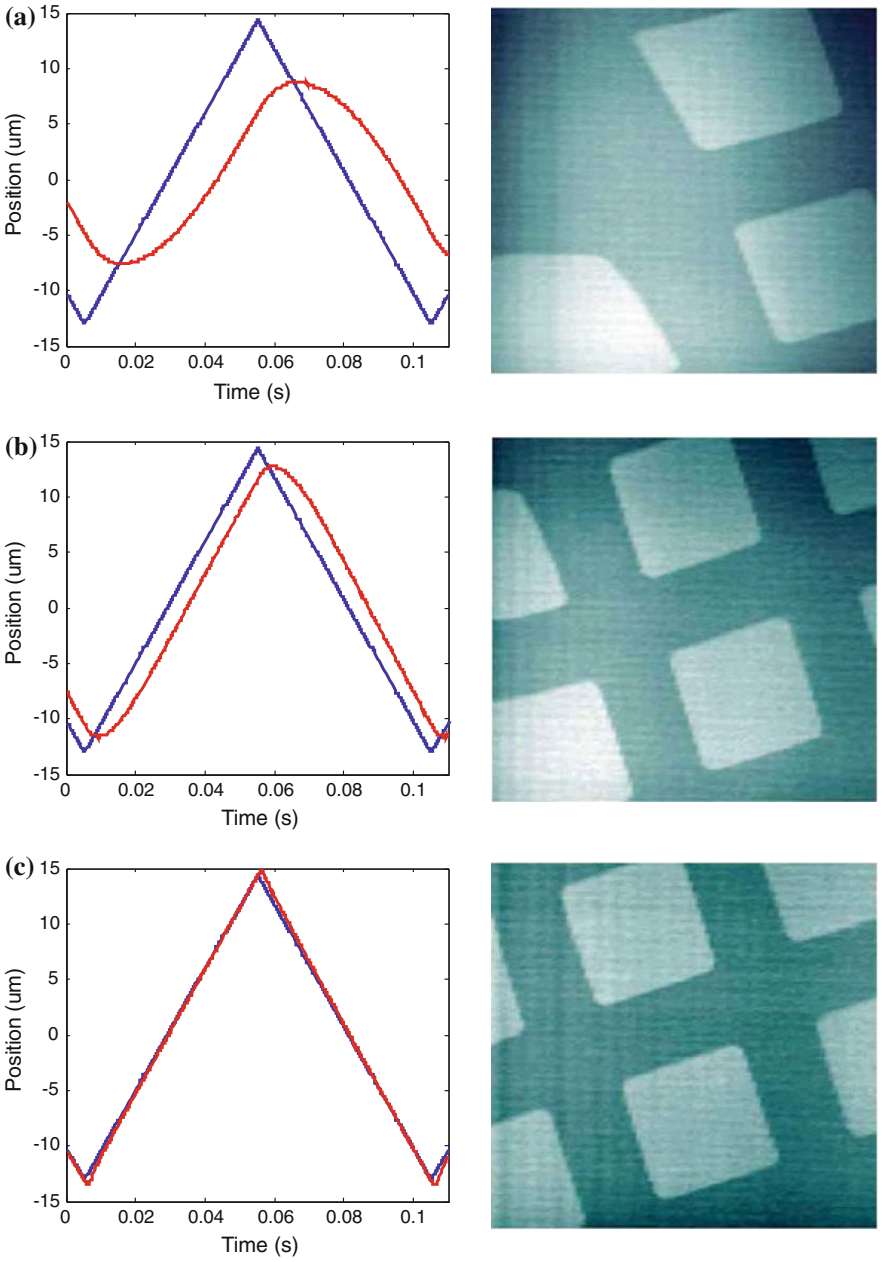

Fig. 7.19 The x-axis scanning performance and resulting image for each of the three controller strategies. The scanning trajectory is a full-range (27 μm) 10 Hz *triangle wave*. **a** PI control, **b** PI + notch, **c** PI + IRC damping

implementation is simplified. Third, compared to model-based feedforward approaches (Clayton et al. 2009; Croft et al. 2001), RC does not require extensive modeling of the system. Due to variations in the system dynamics, for example due to aging (Lowrie et al. 1999) or temperature variations (Lee and Saravanos 1998), open-loop feedforward approaches often lack robustness. On the other hand, the feedback mechanism built into RC provides robustness to parameter variation. Finally, RC can be easily implemented digitally, and thus high-speed data acquisition and control hardware such as field-programmable gate array systems (Fantner et al. 2005) can take advantage of the RC structure for precision control. It has also recently been demonstrated that RC can also be implemented using a single FIR filter which dramatically simplifies the implementation (Teo and Fleming 2014).

7.10.2 Repetitive Control Concept and Stability Considerations

To illustrate the concept of RC, consider an example of the discrete-time RC closed-loop system shown in Fig. 7.20a. The dynamics of the nanopositioner, assumed to be linear, is represented by $G_p(z)$, where $z = e^{j\omega T_s}$, $\omega \in (0, \pi/T_s)$. In the block diagram, $G_c(z)$ is a feedback controller, such as an existing PID controller; $Q(z)$ is a low-pass filter for robustness; k_{rc} is the RC gain; and $P_1(z) = z^{m_1}$ and $P_2(z) = z^{m_2}$, where m_1, m_2 are non-negative integers, are positive phase lead compensators to enhance the performance of the RC feedback system. It is emphasized that the phase lead compensators z^{m_1} and z^{m_2} provide a linear phase lead of (in units of radians)

$$\theta_{1,2}(\omega) = m_{1,2} T_s \omega, \text{ for } \omega \in (0, \pi/T_s). \tag{7.27}$$

The key component of the repetitive controller is the signal generator. To create a signal generator with period T_p, the inner loop contains the pure delay z^{-N}, where the positive integer $N = T_p/T_s$ is the number of points per period T_p; and T_s is the sampling time. An analysis of the performance of the closed-loop system is presented below, where the following assumptions are considered: (1) the reference trajectory $R(z)$ is periodic and has period T_p and (2) the closed-loop system without the RC loop is asymptotically stable, i.e., $1 + G_c(z)G_p(z) = 0$ has no roots outside of the unit circle in the z-plane.

Assumptions 1 and 2 are easily met for many applications in nanopositioning, including SPMs. For example in AFM imaging, the lateral movements of the piezoactuator are periodic, such as a triangle scanning signal. Also, most SPMs are equipped with feedback controllers $G_c(z)$ to control the lateral positioning, which can be tuned to be stable.

The transfer function of the signal generator [or RC block, Fig. 7.20a] that relates $E(z)$ to $A(z)$ is given by

$$\frac{A(z)}{E(z)} = \frac{Q(z)P_1(z)z^{-N}}{1 - Q(z)P_1(z)z^{-N}} = \frac{Q(z)z^{(-N+m_1)}}{1 - Q(z)z^{(-N+m_1)}}. \tag{7.28}$$

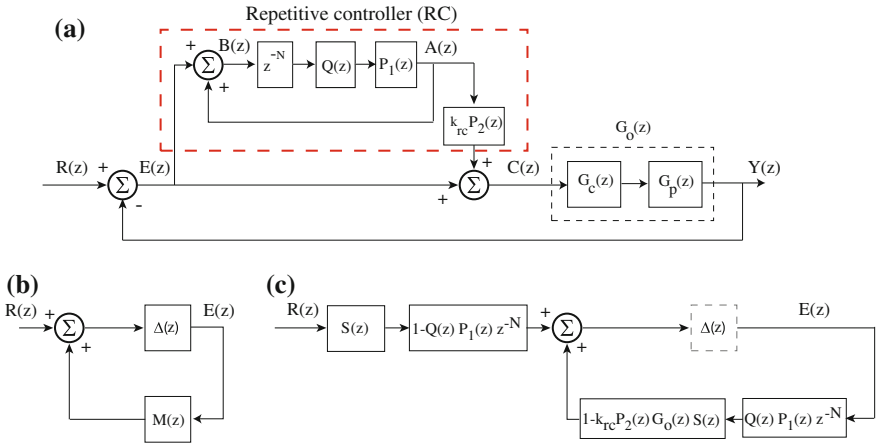

Fig. 7.20 The repetitive control (RC) feedback system. **a** The block diagram of the proposed RC system. **b** Positive feedback system for stability analysis. **c** Positive feedback system representing the block diagram in part **a** for stability analysis

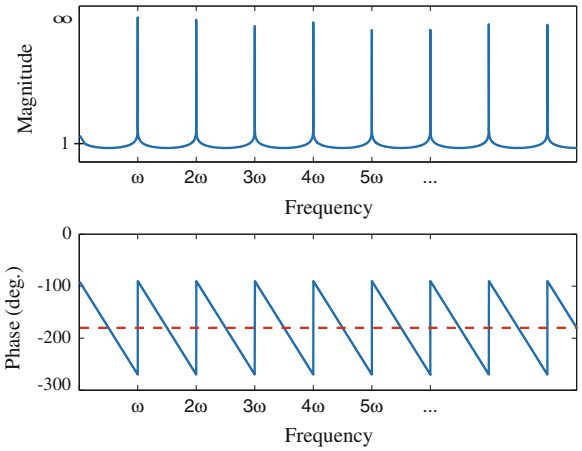

Fig. 7.21 Magnitude and phase versus frequency for signal generator $z^{-N}/(1 - z^{-N})$, where $z = e^{j\omega T_s}$

In the absence of both the low-pass filter $Q(z)$ and positive phase lead $P_1(z) = z^{m_1}$, the poles of the signal generator are $1 - z^{-N} = 0$; therefore, the frequency response of the signal generator shown in Fig. 7.21 reveals infinite gain at the fundamental frequency and its harmonics $\omega = 2n\pi/T_p$, where $n = 1, 2, 3, \ldots$. The infinite gain at the harmonics is what gives the RC its ability to track a periodic reference trajectory. As a result, RC is a useful control method for applications such as SPM in which the scanning motion is repetitive. Unfortunately, the RC also contributes phase lag which causes instability. Therefore, the stability, robustness, and tracking performance of

the RC closed-loop system must be carefully considered. In the following, these issues will be addressed, and the conditions for how to choose the RC gain k_{rc} are presented, along with a discussion of the effects of the phase lead compensators $P_1(z)$ and $P_2(z)$ on the performance of the closed-loop system.

To analyze the stability of the closed-loop RC system shown in Fig. 7.20a, consider the transfer function relating the reference trajectory $R(z)$ and the tracking error $E(z)$,

$$\frac{E(z)}{R(z)} = \frac{1 - H(z)}{1 - H(z) + \big[(k_{\text{rc}} P_2(z) - 1)H(z) + 1\big]G_o(z)}, \tag{7.29}$$

where $H(z) = Q(z)z^{(-N+m_1)}$ and $G_o(z) = G_c(z)G_p(z)$. Multiplying the numerator and denominator of (7.29) by the sensitivity function $S(z) = 1/(1 + G_o(z))$ of the feedback system without the repetitive controller, the following transfer function is obtained:

$$S_{\text{rc}}(z) = \frac{E(z)}{R(z)} = \frac{\big[1 - H(z)\big]S(z)}{1 - H(z)\big[1 - k_{\text{rc}} P_2(z)G_o(z)S(z)\big]}. \tag{7.30}$$

The $S_{\text{rc}}(z)$ shown above is referred to as the sensitivity function of the closed-loop RC system.

The stability conditions for the RC system can be determined by simplifying the block diagram in Fig. 7.20a to the equivalent interconnected system shown in Fig. 7.20b, which results in Fig. 7.20c. Then the RC sensitivity transfer function (7.30) can be associated with the $M(z)$ and $\Delta(z)$ terms in Fig. 7.20c for stability analysis.

Because the closed-loop system without the RC loop is assumed to be asymptotically stable, then the sensitivity function without RC, $S(z)$, has no poles outside the unit circle in the z-plane, so it is stable. Likewise, $1 - H(z)$ is required to be bounded input - bounded output stable. Replacing $z = e^{j\omega T_s}$, the positive feedback closed-loop system in Fig. 7.20c is internally stable according to The Small Gain Theorem (Zhou and Doyle 1998) when

$$\begin{aligned} &\big|H(z)\big[1 - k_{\text{rc}} P_2(z)G_o(z)S(z)\big]\big| = \\ &\quad \Big|H(e^{j\omega T_s})\big[1 - k_{\text{rc}} e^{j\theta_2(\omega)} G_o(e^{j\omega T_s})S(e^{j\omega T_s})\big]\Big| < 1, \end{aligned} \tag{7.31}$$

for all $\omega \in (0, \frac{\pi}{T_s})$, where the phase lead $\theta_2(\omega)$ is defined by Eq. (7.27). By satisfying condition (7.31), the closed-loop RC system shown in Fig. 7.20a is asymptotically stable.

In general, both the RC gain k_{rc} and the phase lead $\theta_2(\omega)$ affect the stability and robustness of RC as well as the rate of convergence of the tracking error. In the following, condition (7.31) is used to determine explicitly the range of acceptable k_{rc} for a given $Q(z)$ and $G_o(z)$. The effects of the phase lead $\theta_2(\omega)$ on robustness and the phase lead $\theta_1(\omega)$ on the tracking performance will be discussed next.

Let $T(z)$ represent the complementary sensitivity function of the closed-loop feedback system without RC, that is, $T(z) = G_o(z)S(z)$. Suppose the magnitude of the low-pass filter $|Q(z)|$ approaches unity at low frequencies and zero at high frequencies, hence $|Q(e^{j\omega T_s})| \leq 1$, for $\omega \in (0, \pi/T_s)$. Therefore, condition (7.31) becomes

$$\left|1 - k_{\text{rc}} e^{j\theta_2(\omega)} T(e^{j\omega T_s})\right| < 1 \leq \frac{1}{|Q(e^{j\omega T_s})|}. \tag{7.32}$$

Replacing the complementary sensitive function with $T(e^{j\omega T_s}) = A(\omega)e^{j\theta_T(\omega)}$, where $A(\omega) > 0$ and $\theta_T(\omega)$ are the magnitude and phase of $T(e^{j\omega T_s})$, respectively, Eq. (7.32) becomes

$$\left|1 - k_{\text{rc}} A(\omega) e^{j[\theta_T(\omega)+\theta_2(\omega)]}\right| < 1. \tag{7.33}$$

Finally, solving Eq. (7.33) leads to the following two conditions for the RC gain k_{rc} and linear phase lead $\theta_2(\omega)$ to ensure stability:

$$0 < k_{\text{rc}} < \frac{2\cos[\theta_T(\omega) + \theta_2(\omega)]}{A(\omega)} \quad \text{and} \tag{7.34}$$

$$-\pi/2 < [\theta_T(\omega) + \theta_2(\omega)] < \pi/2. \tag{7.35}$$

By Eq. (7.35), the lead compensator $P_2(z) = z^{m_2}$ accounts for the phase lag of the closed-loop feedback system without RC. In fact, $P_2(z)$ enhances the stability margin of the closed-loop RC system by increasing the frequency at which the phase angle crosses the $\pm 90°$ boundary. This frequency will be referred to as the crossover frequency.

7.10.3 Dual-Stage Repetitive Control

The challenges with designing and implementing RC include stability, robustness, and achieving good steady-state tracking performance. One solution to the stability and robustness problem is to incorporate a low-pass filter into the RC loop (Tomizuka et al. 1998) or employ a simple frequency aliasing filter (Ratcliffe 2005). It is pointed out that a tradeoff is made between robustness and high-frequency tracking when such filters are used. The steady-state tracking performance of RC can be improved as shown above, for example by cascading a phase-lead compensator to account for the phase lag of the low-pass filter to increase the controller gain at the harmonics of the reference trajectory (Broberg and Molyet 1994; Aridogan et al. 2009). High-order RC has been studied in (Steinbuch et al. 2007) to improve performance and robustness in the presence of noise and variations in the signal period.

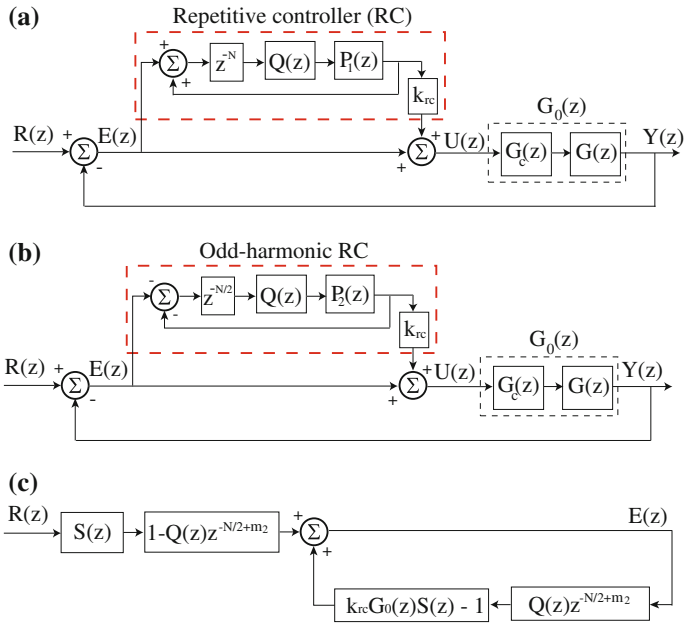

Fig. 7.22 **a** A conventional RC system, where the $R(z)$ represents a periodic reference trajectory, $Y(z)$ is the system output, $G_c(z)$ is the controller and $G(z)$ is the plant dynamics. **b** An odd-harmonic RC with a linear phase-lead compensator $P_2(z) = z^{m_2}$ and a RC gain k_{rc} to enhance performance. **c** An equivalent block diagram of (**b**) for stability analysis

Dual-stage repetitive control (dual-RC) can be used to further improve tracking performance. The dual-RC design is motivated by the need to further reduce the magnitude of the sensitivity function of the closed-loop system to help lower the tracking error. This is achieved by cascading a conventional RC with an odd-harmonic RC (Zhou et al. 2007; Shan and Leang 2012a), effectively '*squaring*' the controller. This structure not only lowers the tracking error compared to conventional RC, but also offers good robustness for tracking odd-harmonic trajectories. It is noted that a similar dual-RC structure has been studied in (Kim and Tsao 2004), where two identical RCs are cascaded together (series connection); and a parallel configuration is presented in (Zhou et al. 2007). In contrast, the proposed dual-RC cascades an enhanced conventional RC with an odd-harmonic RC, and the series configuration is specifically tailored for tracking periodic scanning trajectories such as triangle signals with odd harmonics. Such reference signals are commonly used in piezo-based nanopositioners for raster-type and scanning applications, like AFM imaging.

The tracking performance of the conventional RC system shown in Fig. 7.22a is governed by the sensitivity function

$$S_{\text{rc}}(z) \triangleq \frac{E(z)}{R(z)} = \frac{[1 - H_1(z)]S(z)}{1 - H_1(z)[1 - k_{\text{rc}}G_0(z)S(z)]}, \tag{7.36}$$

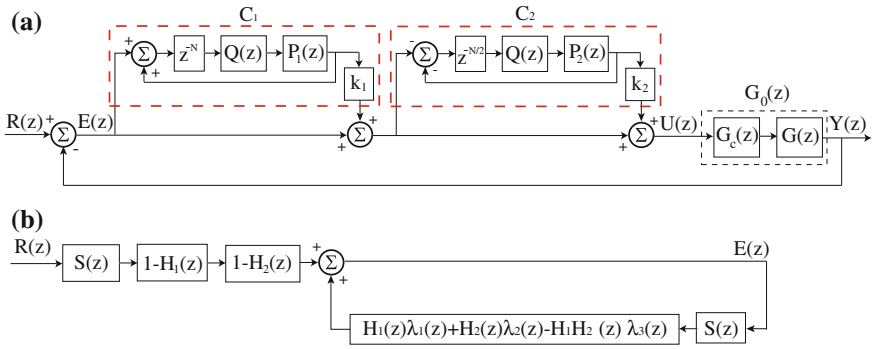

Fig. 7.23 **a** A dual-stage RC design consisting of a conventional RC (C_1) cascaded with an odd-harmonic RC (C_2) and **b** the equivalent block diagram of (**a**) for stability analysis

where $H_1(z) = Q(z)z^{-N+m_1}$ and $S(z) = 1/[1 + G_0(z)]$ is the sensitivity function of the feedback system without the repetitive controller. One approach to improve the tracking performance of the conventional RC is to reduce the magnitude of S_{rc} by cascading together two signal generators, effectively producing a squaring effect (Kim and Tsao 2004). However, the reference trajectories used in the scanning operation in SPMs are generally odd-harmonic signals (e.g., triangle trajectories), it is preferred that an odd-harmonic RC (Zhou et al. 2007) as depicted in Fig. 7.22b be cascaded with a conventional RC as shown in Fig. 7.23a, instead of cascading two conventional RCs. By doing this, the resultant sensitivity function is

$$\widetilde{S}_{\text{rc}}(z) = \frac{[1 - H_1(z)][1 - H_2(z)]}{W(z) + [1 - H_1(z)(1 - k_1)][1 - H_2(z)(1 - k_2)]G_0(z)}, \tag{7.37}$$

where $W(z) = [1-H_1(z)][1-H_2(z)]$ and $H_2(z) = -z^{-\frac{N}{2}+m_2}Q(z)$. The advantage of the enhanced dual-RC design over cascading two conventional RCs together is added performance and robustness. Cascading two conventional RCs together results in excessive gain at the even harmonics, which can degrade the system's performance for tracking odd-harmonic reference trajectories (Costa-Castello et al. 2004). The performance of the enhanced dual-RC is illustrated by comparing the magnitude response of the sensitivity function $\widetilde{S}_{\text{rc}}(z)$ of the enhanced dual-RC in Eq. (7.37) to the magnitude response of the sensitivity function $S_{\text{rc}}(z)$ of the conventional RC in Eq. (7.36) and the sensitivity function $\overline{S}_{\text{rc}}(z)$ of the odd-harmonic RC in Fig. 7.22b, given by

$$\overline{S}_{\text{rc}}(z) = \frac{[1 - H_2(z)]S(z)}{1 - H_2(z)[1 - k_{\text{rc}}G_0(z)S(z)]}. \tag{7.38}$$

The comparison of the three RC configurations is shown in Fig. 7.24, where the frequency response functions are generated in Matlab using the '`margin`' command

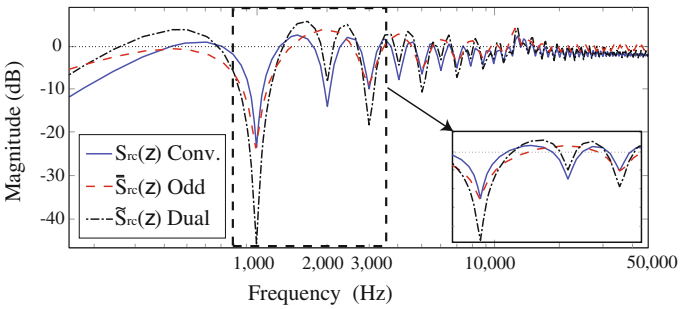

Fig. 7.24 Comparison of magnitude versus frequency plots for the sensitivity functions for different RC configurations, where $S_{\text{rc}}(z)$ denotes the conventional RC (*solid line*), $\bar{S}_{\text{rc}}(z)$ is for the odd-harmonic RC (*dash line*), and $\tilde{S}_{\text{rc}}(z)$ represents the dual RC (*dash-dot line*)

using $N = 100, m_1 = m_2 = 0, Q(z) = 1$, and $T_s = 10\,\mu s$ as an illustrative example. The results reveal that the odd-harmonic RC has little affect on the even-harmonics like the conventional RC (gain at first even harmonic: -13.7 dB for conventional RC, 4.49 dB for odd-harmonic RC, and -8.69 dB for dual-RC). Instead, the magnitude of the sensitivity function for the dual-RC is significantly lower than the conventional RC at the odd-harmonics (-24.4 dB for conventional RC vs. -47.1 dB for dual-RC at the first odd harmonic). This implies that (1) the odd-harmonic RC has the same tracking performance as the conventional RC for tracking odd-harmonic trajectories but it provides the system with more robustness by reducing the gain at the even harmonics, which effectively minimizes the amplification of signals in that frequency range, such as noise and (2) the dual-RC provides higher gain than the conventional RC at the odd-harmonics; therefore, the dual-RC will improve the tracking of trajectories with odd-harmonics.

The stability conditions for the dual-RC is presented as follows. First, the stability conditions for the odd-harmonic RC is presented, then the conditions for the dual-RC is presented. Readers are referred to Shan and Leang (Shan and Leang 2012a) for details of the stability analysis and proof.

Let T_s be the sampling time. Consider the odd-harmonic RC shown in Fig. 7.22b and the following assumptions: (1) the reference trajectory $R(z)$ is periodic in time with period T_p and (2) the closed-loop system without the RC is asymptotically stable, i.e., $1 + G_0(z) = 0$ has no roots outside of the unit circle in the z-plane. For the odd-harmonic RC, if Assumptions 1 and 2 hold and if $|Q(e^{j\omega T_s})| \leq 1$ and

$$0 < k_{\text{rc}} < \frac{2\cos[\theta_T(\omega)]}{A(\omega)} \text{ and } -\pi/2 < \theta_T(\omega) < \pi/2, \tag{7.39}$$

for $\omega \in (0, \pi/T_s)$, then the odd-harmonic RC feedback system shown in Fig. 7.22b is asymptotically stable. This result states that within an acceptable operating frequency range, there exists a sufficiently small RC gain k_{rc} such that the closed-loop

odd-harmonic RC system is stable. Next, the stability conditions for the dual-RC, created by cascading an odd-harmonic RC with the conventional RC, is presented.

Consider the enhanced dual-RC system shown in Fig. 7.23a. If Assumptions 1 and 2 hold and if $|Q(e^{j\omega T_s})| \leq 1$ and

$$\frac{3\cos[\theta_T(\omega)] - \Delta}{3A(\omega)} < k_1, k_2 < 1 + \sqrt{1 + \frac{3\cos[\theta_T(\omega)] + \Delta}{3A(\omega)}},$$
$$-\pi/9 \leq \theta_T(\omega) \leq \pi/9, \tag{7.40}$$

with $\Delta = \sqrt{9\cos^2[\theta_T(\omega)] - 8}$ for $\omega \in (0, \pi/T_s)$, then the closed-loop system in Fig. 7.23a is asymptotically stable (see Shan and Leang (2012a) for details of the stability analysis and proof). Therefore by satisfying the above conditions, that is by picking appropriate values for the RC gains, k_1 and k_2, within a particular operating frequency range, the dual-RC is guaranteed stable.

7.10.4 Handling Hysteresis

In the above analysis, the effects of hysteresis were not considered explicitly in the RC design. Hysteresis can drastically affect the performance of a closed-loop controller, particularly if the controller is designed around a linear dynamics model (Main and Garcia 1997). To keep the analysis simple, an approach to minimize the affect of hysteresis for RC is optimizing the resident feedback controller $G_c(z)$ in such a way that the closed-loop performance accounts for the hysteresis behavior over the bandwidth of interest. Additionally, it has been shown that high-gain feedback control is effective for significantly reducing hysteresis behavior (Leang and Devasia 2007). Another approach is depicted in Fig. 7.25a, where an internal feedback loop is used to linearize the plant dynamics (Choi et al. 2002). Recently in (Shan and Leang 2012b) the design of RC which factors in the hysteresis effect was studied. If the hysteresis nonlinearity exceeds a particular bound, the hysteresis can be accounted for using model-based feedforward compensation as illustrated in Fig. 7.25b (Ahn 2003; Shan and Leang 2012a, b) (see Chap. 11). Therefore, compensating for the hysteresis effect permits the application of the analysis presented above.

7.10.5 Design and Implementation

Two repetitive controllers were designed, implemented, and their responses were compared to PID control. The first was a standard RC with a low-pass filter $Q(z)$ in the RC loop. The standard RC did not include phase lead compensators. The second RC contained the two phase lead compensators z^{m_1} and z^{m_2} to improve the

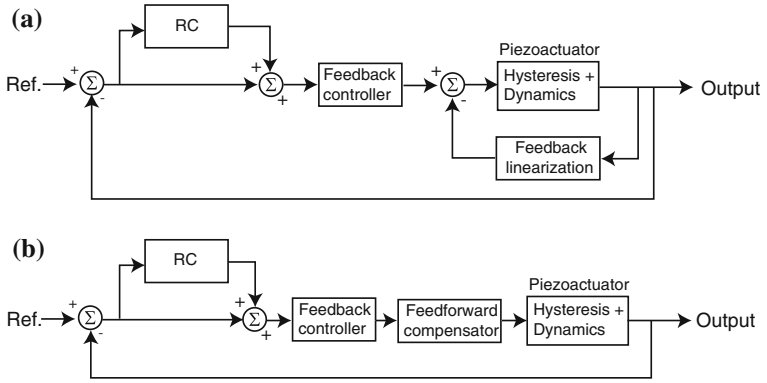

Fig. 7.25 Techniques to account for hysteresis in RC design. **a** feedback-linearization approach and **b** feedforward hysteresis compensation (Shan and Leang 2012a, b)

tracking performance and stability, respectively. The details of the design process are described below.

The experimental AFM system (Molecular Imaging PicoPlus model) and block diagram of the control system are shown in Fig. 7.26a, b, respectively. The AFM uses a piezoelectric tube-shaped actuator for positioning the cantilever and probe tip. The AFM was customized to permit the application of control signals to control the movement of the piezoactuator in the three coordinate axes (x, y, and z). Inductive sensors were used to measure the displacements of the piezoactuator and the signals were accessible through a custom signal access module. The gain of the inductive sensors were 96–97 μm/V in the x-axis and y-axis, respectively. A PC computer and data acquisition system running custom C code were used to implement the RC control system. The sampling frequency of the data acquisition and control hardware was 10 kHz.

The RC was applied to track a periodic reference trajectory in the x-axis as an illustrative example. This axis was the fast-scanning axis because the probe tip was moved back and forth at least 100 times faster than the up and down motion in the y-direction during imaging. For example, a 100×100 pixel image requires the AFM tip to scan back and forth across the sample surface 100 times and slowly move from top to bottom. It is noted that the effects due to cross-coupling in piezo-tube actuators were not considered in this work. Interested readers are referred to the work of Tien et al. (2005), for additional details to further improve tracking performance.

A linear dynamics model for the piezoactuator was obtained for designing the RC system. The model was found by curve fitting the measured frequency response function. The frequency response along the x axis was measured using a dynamic signal analyzer (DSA, Hewlett Packard, Model 35670A). The response was measured over small ranges to minimize the effects of hysteresis and above 1 Hz to avoid the effects of creep (Croft et al. 2001). The resulting frequency response curves are shown in Fig. 7.27. A linear 12th-order transfer function model $G(s)$ (dash-dot line

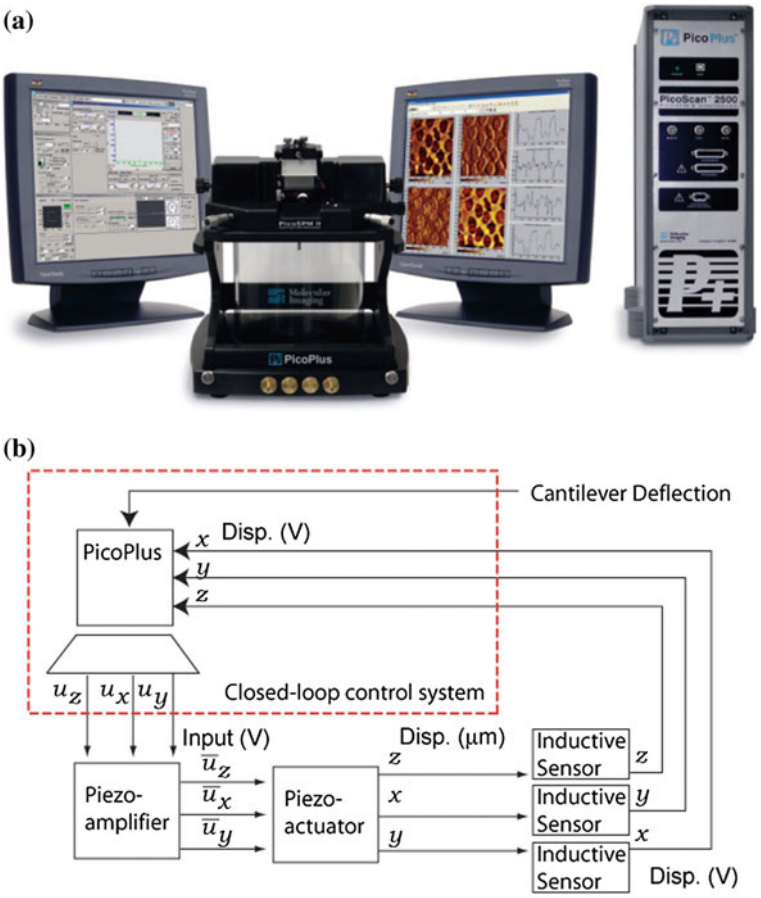

Fig. 7.26 **a** The AFM system and **b** a block diagram of the AFM and control system. An external computer running custom C code was used to implement the control algorithm

in Fig. 7.27) was curve fitted to the measured frequency response function. The continuous-time model was then converted to the discrete-time model $G_p(z)$ using the Matlab function `c2d` with a sampling frequency of 10 kHz (shown by the dashed line in Fig. 7.27).

Prior to integrating the RC, a PID controller was designed for the piezoactuator to control the motion along the x axis. The PID controller is given by

$$G_c(z) = K_p + K_i \left(\frac{z}{z-1} \right) + K_d \left(\frac{z-1}{z} \right), \tag{7.41}$$

where the Ziegler-Nichols method (Franklin et al. 2006) was used to tune the parameters of the controller to $K_p = 1$, $K_i = 1450$, and $K_d = 0.0002$. The PID controller

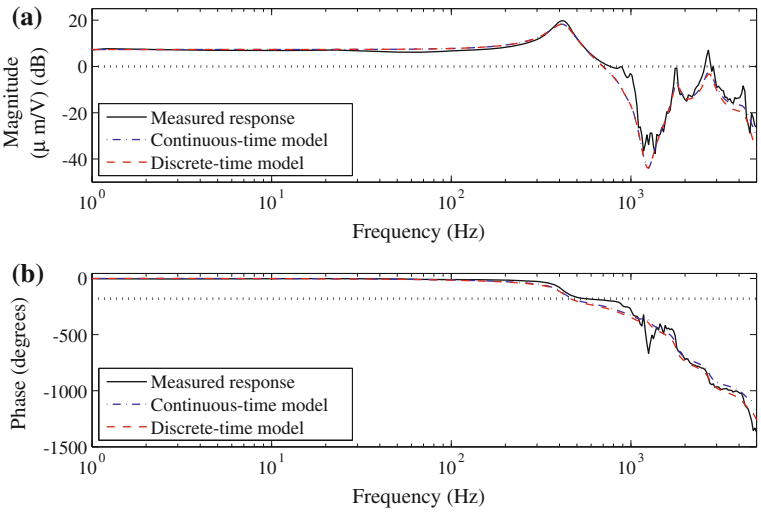

Fig. 7.27 The frequency response of piezoactuator along the x axis. The *solid line* is the measured response; the *dash-dot* line represents the linear continuous-time model $G(s)$; and the *dash line* is the linear discrete-time model $G_p(z)$ using Matlab function `c2d` with zero-order hold and sampling frequency of 10 kHz

was implemented at a sampling frequency of 10 kHz. The performance of the PID controller to a step reference is shown in Fig. 7.28a. It can be observed that without PID control, the open-loop response shows significant overshoot. Also, after 30 ms creep effect becomes noticeable. Creep is a slow behavior and after several minutes the tracking error can be in excess of 20 % (Leang and Devasia 2006). On the other hand, the PID controller minimized the overshoot and creep effect.

The response of the PID controller for tracking a triangular trajectory at 1, 5, and 25 Hz are shown in Fig. 7.28b. Triangle reference signals are commonly used in AFM imaging. The maximum tracking error for the three cases are shown in Fig. 7.28c. The error at 1 Hz (low speed) was relatively small, approximately 1.48 % of the 10-μm range (±5 μm). However, at 25 Hz (high speed) scanning the error was unacceptably large at 10.70 %. Due to vibrational dynamics and hysteresis effects, open-loop AFM imaging is limited to less than 2–3 Hz. The objective was to reduce the tracking error by adding a repetitive controller to the PID loop.

The next steps are to design the low-pass filter and phase lead z^{m_2} for stability and robustness, followed by designing the phase lead z^{m_1} to minimize the steady-state tracking error. The steps are outlined as follows:

First, the RC was designed for stability and robustness. This involves designing a low-pass filter $Q(z)$ and adding phase lead via m_2 to satisfy the conditions given by Eqs. (7.34) and (7.35). The following low-pass filter was used in the RC loop,

$$Q(z) = \frac{a}{z+b}, \tag{7.42}$$

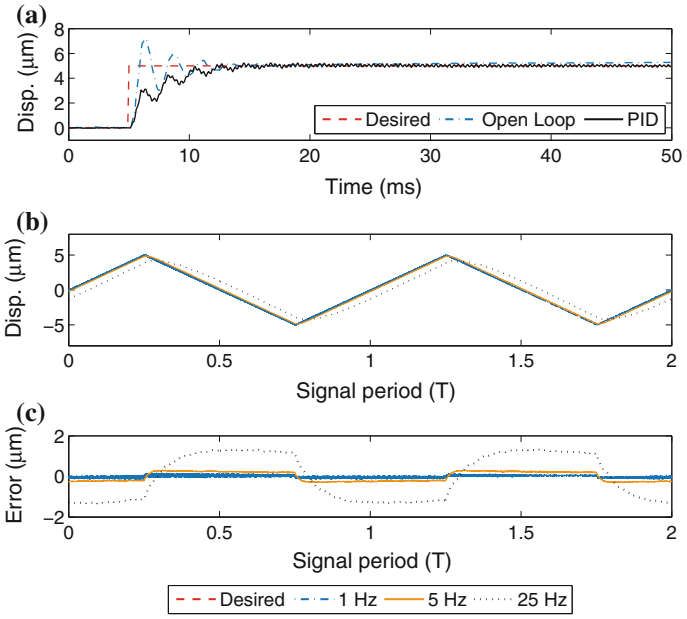

Fig. 7.28 The measured responses of the PID controller to **a** a step reference and **b** triangle references at 1, 5, and 25 Hz. **c** The tracking error for the triangle reference signals associated with plot (**b**)

where $|a| + |b| = 1$. The cutoff frequency ω_Q of the low-pass filter was chosen below the $\pm 90°$ crossover frequency to satisfy Eq. (7.35). The low-pass filter cutoff frequency is limited by the crossover frequency. Also, the cutoff frequency limits the achievable scan rate to about one-tenth of the cutoff frequency, i.e., $\omega_Q/10$.

The phase response $\theta_T(\omega)$, of the closed-loop feedback system without RC, and different phase lead $\theta_2(\omega)$ are shown in Fig. 7.29. Without phase lead ($m_2 = 0$), the $\pm 90°$ crossover frequency was approximately 486 Hz. This value sets the maximum cutoff frequency for the low-pass filter and the maximum scan rate.

Next, simulations were done to show the tracking performance of RC. The chosen cutoff frequency for $Q(z)$ was 250 Hz and zero phase lead ($m_2 = 0$) was used. Therefore, the maximum scan rate is 25 Hz. It is noted that for higher rate scanning, the cutoff can be increased, but only up to 486 Hz when $m_2 = 0$ (see Fig. 7.29). The 250 Hz cutoff frequency was chosen because it provided a safety margin of approximately two. Then, the RC gain was determined by satisfying Eq. (7.34), for instance picking $k_{rc} = 0.40$. The simulated tracking response for $\pm 25\,\mu$m scan range at 25 Hz is shown in Fig. 7.30. The first two plots, Fig. 7.30a1 and b1, show the tracking performance and error, respectively, for a stable RC system without any phase lead compensators, i.e., $m_1 = m_2 = 0$. In this case, increasing k_{rc} and/or the low-pass filter's cutoff frequency caused instability. Reducing the RC gain, however,

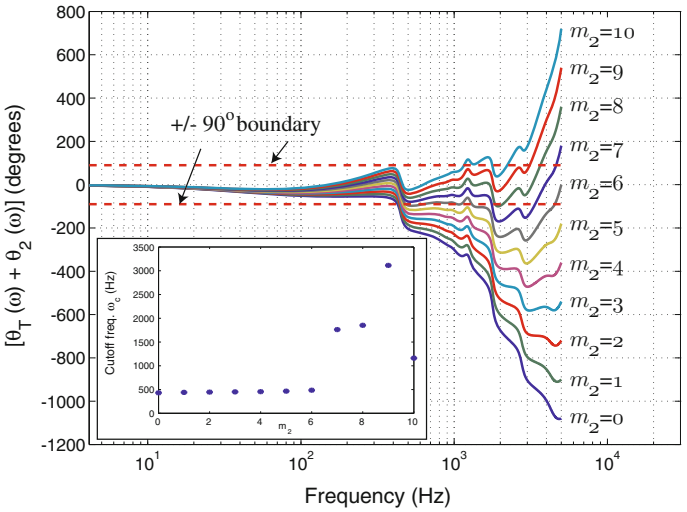

Fig. 7.29 The phase response of the closed-loop feedback system without RC and added phase lead $\theta_2(\omega)$, stability condition Eq. (7.35). The inset plot shows the cutoff frequency versus the phase lead parameter m_2. As m_2 increases, the frequency range for stability increases. A maximum is reached when $m_2 = 9$

reduced the convergence rate. The steady-state tracking error was minimally affected by the RC gain and the phase lead through m_2.

The scan rate can be improved by increasing the $\pm 90°$ crossover frequency by adding phase lead through the parameter m_2. The inset in Fig. 7.29 shows the $\pm 90°$ crossover frequency versus the phase lead parameter m_2.

With the addition of phase lead, such as $m_2 = 7$, the $\pm 90°$ crossover frequency was increased to approximately 2,000 Hz. Therefore, the low-pass filter's cutoff frequency can be improved to raise the RC's bandwidth permitting tracking of higher frequency components. Subsequently, the RC gain Eq. (7.34) can be increased. For example with $m_2 = 7$, $k_{rc} = 1.1$, and simulation results are shown in Fig. 7.30a2, b2 that demonstrate improvement in the convergence rate and reduced tracking error compared to the previous case without phase lead z^{m_2}. As indicated in the inset plot in Fig. 7.29, higher values of m_2 show no improvement in the crossover frequency.

Simulations were done with $k_{rc} = 0.4$ to verify the stability of the closed-loop system with RC for different low-pass filter cutoff frequencies and values of m_2. The results are summarized in Table 7.3. Comparing the inset plot in Fig. 7.29 and the summary in Table 7.3, with $m_2 = 0$ the closed-loop RC system is stable when the low-pass filter frequency is below the crossover frequency of 486 Hz. As the cutoff frequency increases, for example at 500 Hz and above, the RC system is unstable. But the stability can be achieved by adding phase lead through m_2 as shown by the results in Table 7.3.

Finally, by adding phase lead using z^{m_1} in the RC loop, for example $m_1 = 6$, the maximum tracking error, defined as

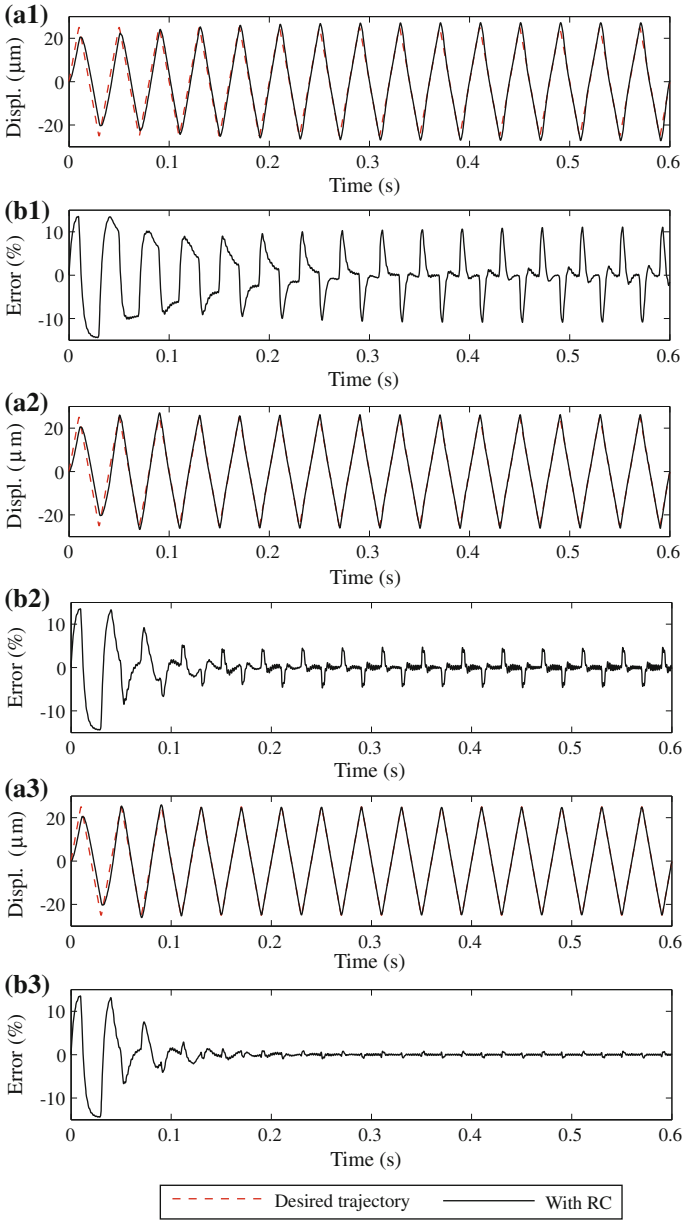

Fig. 7.30 Simulation results showing the tracking performance and error for scanning at 25 Hz, where **a1** and **b1** belong to RC with $k_{rc} = 0.40$ and no phase lead; **a2** and **b2** belong to RC with phase lead $m_2 = 7$ and $k_{rc} = 1.1$; **a3** and **b3** belong to RC with phase leads $m_1 = 6$, $m_2 = 7$ and $k_{rc} = 1.1$

Table 7.3 Stability of RC system for different low-pass filter cutoff frequencies and phase lead z^{m_2}

Phase lead m_2	Low-pass filter $Q(z)$'s cutoff frequency (Hz)				
	250	500	1000	2000	4000
0	Stable	Unstable	Unstable	Unstable	Unstable
2	Stable	Unstable	Unstable	Unstable	Unstable
4	Stable	Stable	Unstable	Unstable	Unstable
6	Stable	Stable	Stable	Unstable	Unstable
8	Stable	Stable	Stable	Stable	Stable

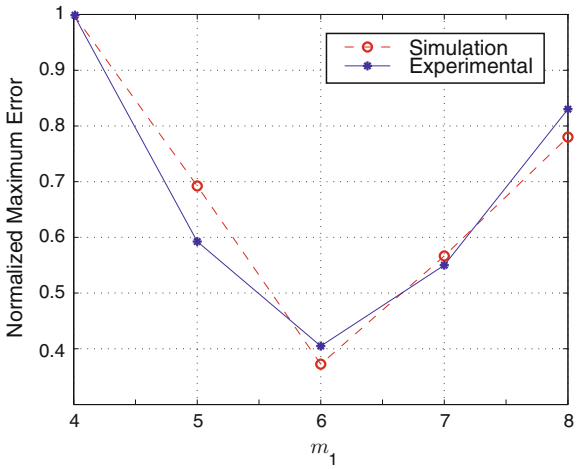

Fig. 7.31 Maximum error versus phase lead parameter m_1. For the experiments, $m_1 = 6$ gave smallest error

$$e_{\max}(\%) = \left[\frac{\max|y-r|}{\max(y)-\min(y)}\right] \times 100\,\%, \tag{7.43}$$

where y and r are the measured and reference outputs, respectively, was substantially reduced from 11.96 and 5.32 % [Fig. 7.30a2, b2] to 0.97 % of the total range (50 μm) as illustrated in Fig. 7.30a3, b3.

The optimum value of the phase lead m_1 was determined by looking at the maximum error versus different m_1 values. The simulation results are shown in Fig. 7.31, plotted as normalized maximum error versus m_1, along with experimental results, which will be discussed in the following section. As shown in the figure, the optimum value is $m_1 = 6$ and this value was also used in the experiments discussed below.

In the experiment, the reference signal was a 25-μm triangle wave at 5, 10, and 25 Hz. The reference trajectory was passed through a two-pole zero-phase-shift filter with cutoff frequency 250 Hz to remove high frequency components before applying it to the closed-loop system. Triangle scan signals are typically used for

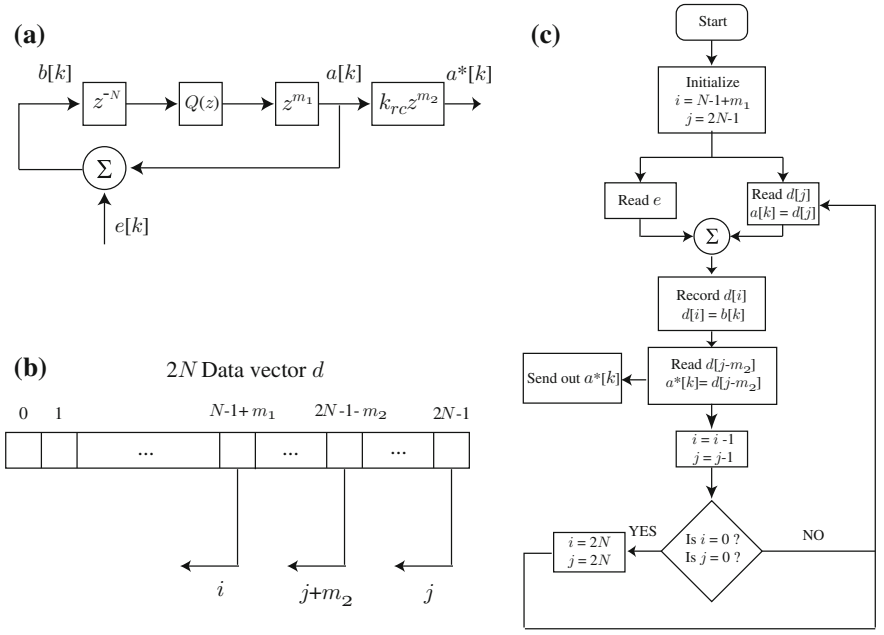

Fig. 7.32 Digital implementation of repetitive control. **a** Equivalent discrete-time block diagram of the RC loop. **b** Linear data vector for implementing the one-period delay and the phase lead compensators. **c** The flow diagram for implementing the RC loop

AFM imaging, and they were filtered to avoid exciting high-frequency dynamics. The cutoff frequency for the low-pass filter $Q(z)$ in the RC loop was set at 250 Hz. Due to hardware limitations where the sampling frequency was 10 kHz, $m_2 = 0$ was chosen to give a maximum scan frequency of 25 Hz. The RC gain was chosen as $k_{\text{rc}} = 0.40$ and this value satisfied the condition given by Eq. (7.34).

Let N be an integer value representing the delay period, the ratio of signal period T_p to the sampling period T_s. Figure 7.32a shows the equivalent discrete-time block diagram for the RC loop, where z^{-N} is a delay of period N. The two phase lead compensators, z^{m_1} and z^{m_2}, had leads of $m_1 = 6$ and $m_2 = 0$. Both the delay and phase leads were implemented using a linear data vector d as shown in Fig. 7.32b with $2N$ elements. Two counters i and j were used, one controlled the location where incoming data was stored to the data vector and the other controlled the location where data was read and sent. The difference in the indices i and j determines the overall delay $-N + m_1 + m_2$, and since $N >> m_1 + m_2$, then the delay implementation is causal. The flow diagram for the RC implementation with respect to the linear data vector d is shown in Fig. 7.32c. Upon reaching the end of the array at $i = 0$ and $j = 0$, both indices were reset to $2N - 1$ and the process was repeated.

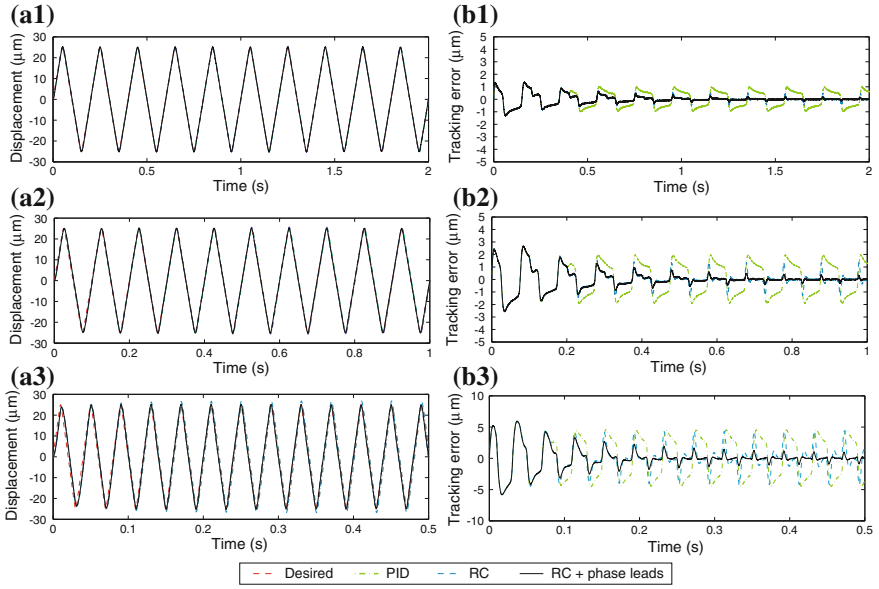

Fig. 7.33 Experimental tracking response and error for PID (*dash-dot*), RC (*dashed line*), and RC with phase lead compensation [$m_1 = 6$ and $m_2 = 0$] (*solid line*) for 5 Hz (**a1** and **b1**), 10 Hz (**a2** and **b2**), and 25 Hz (**a3** and **b3**) scanning

7.10.6 Experimental Results and Discussion

The tracking results for the PID, regular RC, and the RC with the phase lead compensators for ±25-μm scanning at 5, 10, and 25 Hz are presented in Fig. 7.33 and Table 7.4. The steady-state tracking errors, measured at the last two cycles, are reported as a percentage of the range of motion. In particular, the maximum error Eq. (7.43) and the root-mean-squared error defined as

$$e_{\text{rms}}(\%) = \left[\frac{\sqrt{\frac{1}{T}\int_0^T \left[y(t) - r(t)\right]^2 dt}}{\max(y) - \min(y)} \right] \times 100\,\% \tag{7.44}$$

are reported.

Because the action of the repetitive controller is delayed by one scan period, the tracking response for the first period is similar for the PID, RC, and RC with phase lead compensation as shown in Fig. 7.33. However, after the first period, the RC begins to take action as illustrated by reducing tracking error from one cycle to the next. On the other hand, the tracking error of the PID controller persists from one cycle to the next.

The 5 Hz scanning results shown in Fig. 7.33a1, b1 and Table 7.4 demonstrate that the regular RC controller reduced maximum tracking error from 2.01 to 0.96 %

Table 7.4 Tracking results for ±25-μm range

Controller	5 Hz		10 Hz		25 Hz	
	$e_{max}(\%)$	$e_{rms}(\%)$	$e_{max}(\%)$	$e_{rms}(\%)$	$e_{max}(\%)$	$e_{rms}(\%)$
PID	2.01	1.28	3.99	2.61	9.16	6.61
RC	0.96	0.21	2.74	0.79	8.86	3.69
RC + phase leads	0.43	0.08	0.46	0.10	1.78	0.57

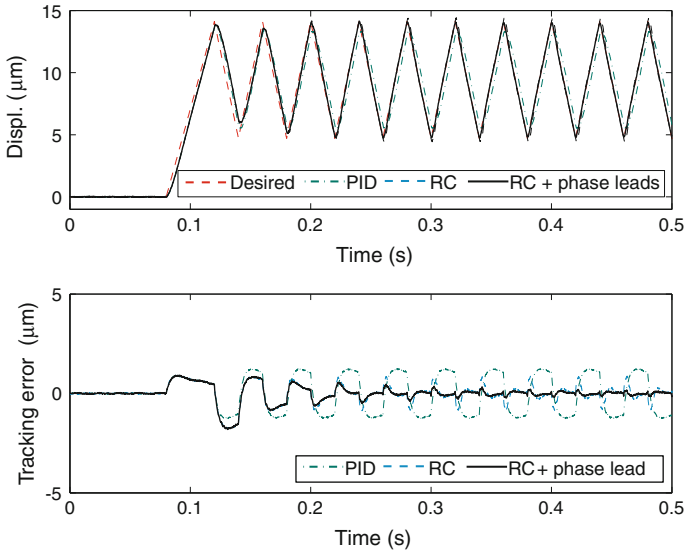

Fig. 7.34 Tracking results for offset triangle scan at 25 Hz

compared to the PID controller, a 52 % reduction. By using RC with the phase lead compensation, an additional 55 % improvement in tracking performance was achieved. In this case, the maximum tracking error is 0.43 %.

At 25 Hz, the tracking error of PID was unacceptable large at 9.16 %. In fact, for AFM scanning operations the maximum tracking error should be less than a few percent. The results in Table 7.4 show that the regular plug-in RC controller was not able to improve the tracking performance at 25 Hz. However, the RC with phase lead compensation gave lower maximum tracking error at 1.78 %. Therefore, the RC with phase lead compensation enables precision tracking at higher scan rates. The optimum value of the phase lead via m_1 was chosen using the simulation results in Fig. 7.31. The simulation results were validated in the experiments as shown in the figure, where $m_1 = 6$ gave the lowest steady-state tracking error.

Finally, scanning offset from the piezoactuator's center position is demonstrated as shown in Fig. 7.34. For this offset scanning operation, the PID controller accounted for the low frequency dynamics such as creep and the RC was used for tracking the

periodic trajectory. The tracking results in Fig. 7.34 show that the RC was effective at minimizing the tracking error.

7.11 Summary

Feedback controllers can be straightforward to design and naturally compensate for many sources of positioning error and nonlinearity. The foremost disadvantage is the need for a position sensor and the possibility of instabilities if plant uncertainty is not taken in account.

This chapter considers three simple controller designs: PI control, inverse control, and IRC damping control. The integral controller was simplest to design and implement but provided the lowest closed-loop bandwidth. An inverse controller (notch filter) can provide much greater bandwidth when the dynamics are well known. However, if the resonance frequency is expected to vary by more than a few percent, the controller must be designed conservatively which can limit the achievable performance.

Integral resonance control (IRC) is a new control strategy that damps the system resonance rather than inverting it. The foremost advantages are simplicity, robustness, and insensitivity to variations in the resonance frequencies. In the experimental comparison, where the resonance frequency varied by 19 %, the settling time of the IRC controller with one-fifth that of the inverse controller.

When the reference trajectory is periodic, RC can significantly improve the tracking performance of a feedback loop. A repetitive controller was combined with a PID feedback system for precise tracking of periodic trajectories with disturbance rejection. Experimental results demonstrate the effectiveness of the RC approach. With a 25 Hz triangular reference signal, the maximum tracking error was less than 2 % using the improved RC technique compared to 9.16 % with standard PID control.

References

Abramovitch DY, Andersson SB, Pao LY, Schitter G (2007) A tutorial on the mechanisms, dynamics, and control of atomic force microscopes. In: Proceeding of American control conference, New York City, pp 3488–3502

Abramovitch DY, Hoen S, Workman R (2008) Semi-automatic tuning of PID gains for atomic force microscopes. In: American control conference, Seattle, pp 2684–2689

Ahn H-S (2003) Design of a repetitive control system for a piezoelectric actuator based on the inverse hysteresis model. In: The fourth international conference on control and automation, pp 128–132

Ando T, Kodera N, Uchihashi T, Miyagi A, Nakakita R, Yamashita H, Matada K (2005) High-speed atomic force microscopy for capturing dynamic behavior of protein molecules at work. e-J Surf Sci Nanotechnol 3:384–392

Ando T, Uchihashi T, Fukuma T (2008) High-speed atomic force microscopy for nano-visualization of dynamic biomolecular processes. Prog Surf Sci 83(7–9):337–437

Aphale SS, Bhikkaji B, Moheimani SOR (2008) Minimizing scanning errors in piezoelectric stack-actuated nanopositioning platforms. IEEE Trans Nanotechnol 7(1):79–90
Aphale SS, Fleming AJ, Moheimani SOR (2007) Integral control of resonant systems with collocated sensor-actuator pairs. IOP Smart Mater Struct 16:439–446
Aridogan U, Shan Y, Leang KK (2009) Design and analysis of discrete-time repetitive control for scanning probe microscopes. ASME J Dyn Syst Meas Control 131:061103 (12 p)
Arimoto S, Kawamura S, Miyazaki F (1984) Bettering operation of robots by learning. J Robot Syst 1(2):123–140
Barrett RC, Quate CF (1991) Optical scan-correction system applied to atomic force microscopy. Rev Sci Instrum 62(6):1393–1399
Bhikkaji B, Moheimani SOR (2008) Integral resonant control of a piezoelectric tube actuator for fast nano-scale positioning. IEEE Trans Mechatron 13(5):530–537
Broberg HL, Molyet RG (1994) A new approach to phase cancellation in repetitive control. In: IEEE industry applications society annual meeting, vol 3, pp 1766–1770
Chen CJ (1992) Electromechanical deflections of piezoelectric tubes with quartered electrodes. Appl Phys Lett 60(1):132–134
Chen S-L, Hsieh T-H (2007) Repetitive control design and implementation for linear motor machine tool. Int J Mach Tools Manuf 47(12–13):1807–1816
Chew KK, Tomizuka M (1990) Digital control of repetitive errors in disk drive systems. IEEE Control Syst Mag 10(1):16–20
Choi GS, Lim YA, Choi GH (2002) Tracking position control of piezoelectric actuators for periodic reference inputs. Mechatronics 12(5):669–684
Clayton GM, Tien S, Leang KK, Zou Q, Devasia S (2009) A review of feedforward control approaches in nanopositioning for high-speed SPM. J Dyn Syst Meas Control 131:061 101(1–19)
Costa-Castello R, Grino R, Fossas E (2004) Odd-harmonic digital repetitive control of a single-phase current active filter. IEEE Trans Power Electron 19(4):1060–1068
Croft D, Shed G, Devasia S (2001) Creep, hysteresis, and vibration compensation for piezoactuators: atomic force microscopy application. ASME Trans, J Dyn Syst Meas Control 123:35–43
Eielsen AA, Burger M, Gravdahl JT, Pettersen KY (2011) Pi^2-controller applied to a piezoelectric nanopositioner using conditional integrators and optimal tuning. In: Proceeding of IFAC World Congress, vol 18, Milano
Fanson JL, Caughey TK (1990) Positive position feedback control for large space structures. AIAA J 28(4):717–724
Fantner GE, Hegarty P, Kindt JH, Schitter G, Cidade GAG, Hansma PK (2005) Data acquisition system for high speed atomic force microscopy. Rev Sci Instrum 76(2):026 118-1–026 118–4
Fleming AJ, Aphale SS, Moheimani SOR (2010) A new method for robust damping and tracking control of scanning probe microscope positioning stages. IEEE Trans Nanotechnol 9(4):438–448
Fleming AJ, Behrens S, Moheimani SOR (2002) Optimization and implementation of multi-mode piezoelectric shunt damping systems. IEEE/ASME Trans Mechatron 7(1):87–94
Fleming AJ, Kenton BJ, Leang KK (2010) Bridging the gap between conventional and video-speed scanning probe microscopes. Ultramicroscopy 110(9):1205–1214
Fleming AJ, Moheimani SOR (2006) Sensorless vibration suppression and scan compensation for piezoelectric tube nanopositioners. IEEE Trans Control Syst Technol 14(1):33–44
Fleming AJ, Wills AG (2009) Optimal periodic trajectories for band-limited systems. IEEE Trans Control Syst Technol 13(3):552–562
Francis BA, Wonham WM (1976) The internal model principle of control theory. Automatica 12(5):457–465
Franklin GF, Powell JD, Emami-Naeini A (2006) Feedback control of dynamic systems, 5th ed. Prentice Hall, Upper Saddle River
Griffith JE, Miller GL, Green CA, Grigg DA, Russell PE (1990) A scanning tunneling microscope with a capacitance based position monitor. J Vac Sci Technol B: Microelectron Nanometer Struct 8(6):2023–2027

Hara S, Yamamoto Y, Omata T, Nakano M (1988) Repetitive control system: a new type servo system for periodic exogenous signals. IEEE Trans Autom Control 33(7):659–668
Humphris ADH, Miles MJ, Hobbs JK (2005) A mechanical microscope: high-speed atomic force microscopy. Appl Phys Lett 86:034 106-1–034 106–3
Inoue T, Nakano M, Iwai S (1981) High accuracy control of a proton synchrotron magnet power supply. In: Proceeding of 8th IFAC World Congress, vol 20, pp 216–221
Kenton BJ, Leang KK (2012) Design and control of a three-axis serial-kinematic high-bandwidth nanopositioner. IEEE/ASME Trans Mechatron 17(2):356–369
Kim B-S, Tsao T-C (2004) A performance enhancement scheme for robust repetitive control system. ASME J Dyn Syst Meas Control 126(1):224–229
Leang KK, Devasia S (2007) Feedback-linearized inverse feedforward for creep, hysteresis, and vibration compensation in afm piezoactuators. IEEE Trans Control Syst Technol 15(5):927–935
Leang KK, Devasia S (2006) Design of hysteresis-compensating iterative learning control for piezo positioners: application to atomic force microscopes. Mechatronics 16(3–4):141–158
Lee H-J, Saravanos DA (1998) The effect of temperature dependent material properties on the response of piezoelectric composite materials. J Intell Mater Syst Struct 9(7):503–508, 1998
Lee C, Salapaka S (August 2009) Fast robust nanopositioning: a linear-matrix-inequalities-based optimal control approach. IEEE/ASME Trans Mechatron 14(4):414–422
Li CJ, Li SY (1996) To improve workpiece roundness in precision diamond turning by in situ measurement and repetitive control. Mechatronics 6(5):523–535
Li Y, Ang KH, Chong G (2006) Pid control system analysis and design. IEEE Control Syst 26(1):32–41
Lowrie F, Cain M, Stewart M, Gee M (1999) Time dependent behaviour of piezo-electric materials. National physical laboratory, Technical report, 151
Main JA, Garcia E (1997) Piezoelectric stack actuators and control system design: strategies and pitfalls. AIAA J Guidance Control Dyn 20(3):479–485
Merry RJE, Ronde MJC, van de Molengraft R, Koops KR, Steinbuch M (2011) Directional repetitive control of a metrological afm. IEEE Trans Control Syst Tech 19(6):1622–1629
Moore KL, Dahleh M, Bhattacharyya SP (1992) Iterative learning control: a survey and new results. J Robot Syst 9(5):563–594
Radmacher M (1997) Measuring the elastic properties of biological samples with the afm. IEEE Eng Med Biol 16:47–57
Ratcliffe JD, Lewin PL, Rogers E (2005) Stable repetitive control by frequency aliasing. In: Intelligent control systems and optimization, pp 323–326
Rost MJ, Crama L, Schakel P, van Tol E, van Velzen-Williams GBEM, Overgauw CF, ter Horst H, Dekker H, Okhuijsen B, Seynen M, Vijftigschild A, Han P, Katan AJ, Schoots K, Schumm R, van Loo W, Oosterkamp TH, Frenken JWM (2005) Scanning probe microscopes go video rate and beyond. Rev Sci Instrum 76(5):053 710-1–053 710-9
Salapaka SM, Salapaka MV (2008) Scanning probe microscopy. IEEE Control Syst Mag 28(2):65–83
Salapaka S, Sebastian A, Cleveland JP, Salapaka MV (2002) High bandwidth nano-positioner: a robust control approach. Rev Sci Instrum 75(9):3232–3241
Schitter G (2009) Improving the speed of AFM by mechatronic design and modern control methods. Tech Mess 76(5):266–273
Schitter G, Åström KJ, DeMartini BE, Thurner PJ, Turner KL, Hansma PK (2007) Design and modeling of a high-speed AFM-scanner. IEEE Trans Control Syst Technol 15(5):906–915
Sebastian A, Pantazi A, Moheimani SOR, Pozidis H, Eleftheriou E (2008) A self servo writing scheme for a MEMS storage device with sub-nanometer precision. In: Proceeding of IFAC World Congress, Seoul, pp 9241–9247
Sebastian A, Salapaka S (2005) Design methodologies for robust nano-positioning. IEEE Trans Control Syst Technol 13(6):868–876
Shan Y, Leang KK (2012a) Accounting for hysteresis in repetitive control design: nanopositioning example. Automatica 48(8):1751–1758

Shan Y, Leang KK (2012b) Dual-stage repetitive control with Prandtl-Ishlinskii hysteresis inversion for piezo-based nanopositioning. Mechatronics 22:271–281
Shan Y, Leang KK (2013) Mechanical design and control for high-speed nanopositioning: serial-kinematic nanopositioners and repetitive control for nanofabrication. IEEE Control Syst Mag (Special Issue on Dynamics and Control of Micro and Naoscale Systems) 33(6):86–105
Steinbuch M, Weiland S, Singh T (2007) Design of noise and period-time robust high-order repetitive control, with application to optical storage. Automatica 43(12):2086–2095
Tamer N, Dahleh M (1994) Feedback control of piezoelectric tube scanners. In: Proceeding of American control conference, Lake Buena Vista, pp 1826–1831
Teo YR, Fleming AJ (2014) A new repetitive control scheme based on non-causal fir filters. In: Proceeding of American control conference, Portland
Tien S, Zou Q, Devasia S (2005) Iterative control of dynamics-coupling-caused errors in piezoscanners during high-speed afm operation. IEEE Trans Control Syst Tech 13(6):921–931
Tomizuka M, Tsao TC, Chew KK (1998) Discrete time domain analysis and synthesis of repetitive controllers. In: American control conference, pp 860–866
Wu Y, Zou Q (2007) Iterative control approach to compensate for both the hysteresis and the dynamics effects of piezo actuators. IEEE Trans Control Syst Technol 15(5):936–944
Wu Y, Zou Q (2009) Robust inversion-based 2-dof control design for output tracking: Piezoelectric-actuator example. IEEE Trans Control Syst Technol 17(5):1069–1082
Zhou K, Wang D, Zhang B, Wang Y, Ferreira JA, de Haan SWH (2007) Dual-mode structure digital repetitive control. Automatica 43:546–554
Zhou K, Doyle JC (1998) Essentials of robust control. Prentice-Hall, Upper Saddle River